Commonalities between robust hybrid incremental nonlinear dynamic inversion and proportional-integral-derivative flight control law design

Pollack, T. S.C.; Theodoulis, S.; van Kampen, E.

DOI
10.1016/j.ast.2024.109377

Publication date
2024

Document Version
Final published version

Published in
Aerospace Science and Technology

Aerospace Science and Technology 152 (2024) 109377

Contents lists available at ScienceDirect

Aerospace Science and Technology

journal homepage: www.elsevier.com/locate/aescte

Commonalities between robust hybrid incremental nonlinear dynamic inversion and proportional-integral-derivative flight control law design

T.S.C. Pollack *, S. Theodoulis, E. van Kampen

Control and Simulation Section, Faculty of Aerospace Engineering, Delft University of Technology, Kluyverweg 1, Delft, 2629HS, Zuid-Holland, the Netherlands

ARTICLE INFO

Communicated by Jérôme Morio

Keywords:
INDI control
PID control
Robust control
Nonlinear control

ABSTRACT

Incremental Nonlinear Dynamic Inversion (INDI) has received substantial interest in the recent years as a nonlinear flight control law design methodology that features inherent robustness against bare airframe aerodynamic variations. However, systematic studies into the robust design benefits of INDI-based control over the classical divide-and-conquer philosophy have been scarce. To bridge this gap, this paper compares the setup of hybrid INDI with a standard industry benchmark that is based on two-degree-of-freedom gain-scheduled proportional-integral-derivative control. This is done on an architectural basis and in terms of achievable robust stability and performance levels with respect to a common set of design requirements. To this end, a non-smooth, multi-objective H_∞-synthesis algorithm is used that incorporates mixed parametric and dynamic uncertainties in the design objective and constraints. It is shown that close similarities exist between hybrid INDI design and gain-scheduled PID control, which leads to virtually equivalent robustness and performance outcomes in both linear time-invariant and linear time-varying contexts. It is therefore concluded that the main benefit of the hybrid INDI does not lie in improved robustness properties *per se*, but in the opportunity to perform modular robust design in an implicit model-following context. Specifically, this implies that the areas of flying qualities, robustness, and nonlinear implementation are directly visible and accessible in the control law structure.

1. Introduction

The majority of flight control laws used by the aerospace industry belong to the class of gain-scheduled proportional-integral-derivative (PID) control with additional filtering and mode logic [1–3]. Engineers use a wide range of design techniques to synthesize PID controllers that meet their design goals and airworthiness requirements. These differ primarily by the type of synthesis technique and how the tuning variables reflect the design objectives. Some examples include linear pole-placement [4,5], LQR/LQG design [1], multi-stage gradient-based optimization [6–8], and formal robust synthesis [9–11]. The nonlinear implementation step or *gain-scheduling* strategy is another aspect that is approached in different ways. This can be achieved by e.g. *a-posteriori* interpolation of local designs or by local optimization of *a-priori* defined global scheduling surfaces. An important concept here is the principle of *local linear equivalence* [12], which ensures that *hidden couplings* [13] induced by the nonlinear plant-controller interconnection are considered appropriately [14–16].

The concept of local synthesis of nonlinear controllers is known as the *divide-and-conquer* design philosophy. Very successful control designs can be obtained with this widely adopted approach. An alternative to this philosophy is the concept of Nonlinear Dynamic Inversion (NDI) [17,18]. The NDI method aims to simplify gain scheduling by *cancelling* the nonlinear bare airframe dynamics. As a result, the flying qualities-dependent and airframe-dependent parts of the control design can be decoupled [19]. This can be viewed as a *modular* approach to control design. As such, NDI-based design has been celebrated for its close connection to the aircraft physics [20–22] and the opportunity to map desired flying qualities directly [19]. This decoupling of design goals within the control law structure is an important benefit, as it contributes to more visible design and therefore a reduction of development complexity [13]. As such, many flight control laws reflect elements of NDI-based design [23]: an example is the crossfeed compensation of nonlinear kinematic couplings in e.g. the EF2000 Eurofighter Typhoon [15,24]. Moreover, a full-authority NDI control law has been incorporated into the F-35 production aircraft [25]. This exemplifies the relevance of NDI in practical flight control design.

The benefits of modularity and visibility notwithstanding, robust design and clearance of NDI controllers still relies on local analysis pro-

* Corresponding author.
E-mail address: t.s.c.pollack@tudelft.nl (T.S.C. Pollack).

https://doi.org/10.1016/j.ast.2024.109377
Received 31 January 2024; Received in revised form 3 July 2024; Accepted 4 July 2024
Available online 9 July 2024

Nomenclature

2DOF	Two-Degree-of-Freedom
(M)CV	(Pitch-axis) Controlled Variable
FCS	Flight Control System
IMF	Implicit Model-Following
(I)(N)DI	(Incremental) (Nonlinear) Dynamic Inversion
IQC	Integral Quadratic Constraint
LPV	Linear Parameter-Varying
LQR	Linear Quadratic Regulator
LQG	Linear Quadratic Gaussian
LTI	Linear Time-Invariant
LTV	Linear Time-Varying
OBM	On-board Model
PID	Proportional-Integral-Derivative
SCF	Scaled Complementary Filter
ZOH	Zero-order Hold

cedures. This is due to the detrimental effects of high-order dynamics [19] and uncertainty [23], for which NDI theory by itself provides no a-priori robustness guarantees [26–28]. This is an important drawback of NDI as a comprehensive design method and relates to the fact that an NDI control law eliminates the bare airframe dynamics by means of an on-board model (OBM) representation of the true airframe dynamics. The impact of discrepancies between this OBM and the real aircraft is of significant concern and has therefore been studied extensively. Outer loop regulation is an important instrument to enhance robustness against these discrepancies. Accordingly, several design guidelines for robust regulation of model-based NDI control laws exist [18,23]. However, these guidelines alone provide no guarantees [28], which implies that the resulting NDI control law must still be analyzed *a-posteriori* for clearance [26,27]. Robust outer loop design based on e.g. μ-synthesis against specified uncertainty sets [29,30] is a significant improvement in this regard.

As an alternative to robust outer loop design procedures, a substantial number of *inner loop* inversion compensation techniques have also been suggested. These concepts aim to explicitly *reduce* model-dependency of the inversion loop and the effects thereof on performance robustness. These range from alternative strategies to estimate the inversion variable [31–33] to on-line system identification [34] and learning [35]. Here, inversion strategies can be classified as purely model-based (MB) [18,36], purely sensor-based (SB) [31,37], or hybrid (HB) [32,33] (which also appears as Robust Multi-Inversion [RMI] in the literature [38,39]). The latter two types result in *incremental* variants of NDI, INDI in short. These incremental variants bypass parts of the OBM by virtue of direct sensor measurements, with the aim to reduce sensitivity to model offsets. The sensor-based concept has received substantial interest in recent years and has been validated in multiple real-world test environments [37,40,41]. However, it was found that this strategy may lead to substantial feedthrough of sensor noise and that it reduces robustness against high-frequency dynamic uncertainty due to its high-gain nature [42]. Moreover, additional challenges arise due to the issue of *synchronization* [43–45]. This relates to the relative timing or phase between the output derivative and input feedback signals. Inadequate consideration of this effect may lead to severe stability issues [42]. These characteristics imply that the lack of a-priori robustness guarantees gets a new dimension. Accordingly, one may require more *balanced* robustness properties from the inversion loop. This is offered by hybrid INDI, which can be viewed as a compromise between the sensor-based and the model-based variants.

Whereas standard (I)NDI theory does not provide a-priori robustness guarantees, robust control synthesis methods such as H_∞ loop-shaping [9,28] or the aforementioned μ-synthesis framework [46] do provide such assurances. These methods incorporate robustness as an integral part of the design process. Many of these synthesis frameworks are based on Linear Time-Invariant (LTI) system considerations; however, formal robust gain scheduled design can be performed as well using Linear Parameter-Varying (LPV) systems theory [12]. Thanks to the development of non-smooth synthesis algorithms [47–49], these robust synthesis frameworks can be exploited to perform systematic, robust design of structured controllers such as gain-scheduled PID control laws. Consequently, these techniques also offer new opportunities for the design of (I)NDI-based control laws. Using this framework, important a-priori robustness guarantees can be obtained for such designs. This does not only concern the outer loop, but the inversion strategy itself as well; however, these opportunities remain largely unexplored still.

In this article, robust synthesis and analysis methods are leveraged to answer the question as to how hybrid INDI design and gain-scheduled PID control compare in the context of robust implicit model-following (IMF) flight control design. Robust H_∞-synthesis principles are leveraged to systematically optimize control law design parameters in terms of LTI robustness and performance against specified (mixed) uncertainty sets. This forms a practical contribution in the context of INDI-based control design. The framework of Integral Quadratic Constraints (IQCs) is used to analyze the resulting designs against the wider class of Linear Time-Varying (LTV) uncertainties. This strategy enables a quantitative comparison of robust stability and performance properties of the said optimized control designs.

The article is structured as follows. First, preliminary design guidelines for robust INDI control are presented in Section 2. A design case study is introduced in Section 3, followed by an outline of the gain-scheduled PID and hybrid INDI control architectures of interest in Section 4. Their similarities will be highlighted first, followed by a description of how the concept of hybrid INDI enables a visible decoupling of flying quality and robustness design goals in an IMF context. Section 5 describes the non-smooth synthesis approach used to synthesize the control laws in terms of robust stability and performance. The results are discussed in Section 6, followed by a reflection on the design guidelines formulated earlier. Finally, the article is concluded in Section 7.

2. Preliminary design guidelines for INDI-based control laws

A number of fundamental linear design principles can be identified for INDI-based control law design. This section covers this aspect in the context of single-channel design. Consider the linear[1] system Σ in state-space format:

$$\Sigma : \begin{cases} \dot{\boldsymbol{x}} &= A\boldsymbol{x} + B\tilde{u} \\ y_{CV} &= C\boldsymbol{x} \end{cases} \tag{1}$$

which is described by the state vector $\boldsymbol{x} \in \mathbb{R}^n$, the input signal $\tilde{u} \in \mathbb{R}$, the controlled variable $y_{CV} \in \mathbb{R}$, and constant matrices A, B, and C. The output dynamics can be formulated as follows:

$$\dot{y}_{CV} = \mathcal{A}\boldsymbol{x} + \mathcal{B}\tilde{u} = \xi + \mathcal{B}\tilde{u} \tag{2}$$

where $\mathcal{A} \triangleq CA$, $\mathcal{B} \triangleq CB$, and $\xi \triangleq \dot{y}_{CV} - \mathcal{B}\tilde{u}$. This formulation is used in anticipation of different inversion strategies, as discussed shortly. Likewise, the following input-output formulation can be written:

$$\dot{y}_{CV}(s) = \left(C[sI - A]^{-1} B\mathcal{B}^{-1} + I\right) \mathcal{B}\tilde{u}(s) \triangleq [P(s) + I]\, \mathcal{B}\tilde{u}(s) \tag{3}$$

[1] This context may lead to the supposition that the insights from this section are limited to INDI in linear form (referred to as IDI) only; however, this limitation does not apply.

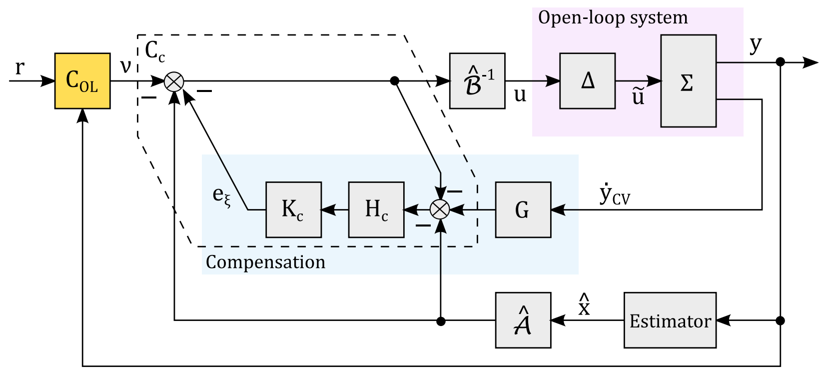

Fig. 1. Hybrid Incremental (Nonlinear) Dynamic Inversion (I[N]DI) control system.

Equations (2) and (3) represent the nominal output dynamics. High-order dynamics and uncertainties are captured through the following extension:

$$\dot{y}_{CV}(s) = G(s)\left(P(s) + I\right)\mathcal{B}\Delta(s)u(s) \tag{4}$$

where G and Δ represent multiplicative known and uncertain dynamic mappings, respectively. Accordingly, $\tilde{u}(s) = \Delta(s)u(s)$.[2] Then, using the state-space model from Equation (2), a Dynamic Inversion (DI) control law can be constructed as follows:

$$u = \hat{\mathcal{B}}^{-1}\left(\nu - \hat{\xi}\right) \tag{5}$$

Here, ν represents the *virtual control* signal generated by an outer loop controller or regulator C_{OL}. The '$\hat{\bullet}$'-notation denotes that only an estimate is available. In the case of ideal inversion, this control law ensures that $\dot{y}_{CV} = \nu$, independent of the bare airframe dynamics.

The type of estimation scheme used to determine $\hat{\xi}$ defines the nature of the DI loop. In a general sense, a scaled, complementary-filtered (SCF) estimation scheme can be used to this end. This scheme represents a combination of the methods proposed by [39,32,33]:

$$\hat{\xi}(s) = K_c H_c(s)\left[G(s)\dot{y}_{CV}(s) - \hat{\mathcal{B}}u(s)\right] + \left[1 - K_c H_c(s)\right]\hat{\mathcal{A}}\hat{x}(s) \tag{6}$$

Here, $K_c \in [0,1]$ is referred to as the *compensation gain* and H_c the *compensation filter*. If $K_c > 0$, an *Incremental* Dynamic Inversion (IDI) control law emerges. This scheme collapses to a purely *model-based* (MB) form if $K_c = 0$, whereas it approaches a purely *sensor-based* (SB) variant if $K_c = 1$ and $H_c \to 1$. For intermediate values of K_c and/or H_c, the inversion is said to be of *hybrid* (HB) nature. This directly extends to the nonlinear case ([I]NDI) as well. The incorporation of the compensation gain K_c in hybrid INDI design has been suggested previously by [32], whereas the complementary filter structure was presented in [33] and closely resembles the concept of Robust Multi-Inversion (RMI) control proposed by [38,39].

An important insight is that Equation (6) can also be formulated as:

$$\begin{aligned}\hat{\xi}(s) &= \hat{\mathcal{A}}\hat{x}(s) + K_c H_c(s)\left[\left(G(s)\dot{y}_{CV}(s) - \hat{\mathcal{B}}u(s)\right) - \hat{\mathcal{A}}\hat{x}(s)\right] \\ &\triangleq \hat{\mathcal{A}}\hat{x}(s) + K_c H_c(s)\bar{e}_{\xi}(s) \triangleq \hat{\mathcal{A}}\hat{x}(s) + e_{\xi}(s)\end{aligned} \tag{7}$$

This shows that hybrid I(N)DI effectively introduces a scaled and filtered inversion error compensation signal e_{ξ} that *corrects* the on-board model (OBM) prediction term $\hat{\mathcal{A}}\hat{x}$. The resulting control system is illustrated in Fig. 1. The compensation gain K_c and filter H_c are key design elements here. Their influence can be further understood through the concept of equivalent regulation, as discussed next.

[2] The 'Δ'-notation must not be confused with the *incremental* notation.

Table 1
Regulation decomposition of $C_c^*(s)$.

Case	Regulation contribution $C_c^*(s)$	Approximation (low ω)
$K_c = 0$	1	1
$K_c < 1$	$K_p^* p_c/z_c(s+z_c)/(s+p_c)$	$\sim K_p^* \quad \omega \in [0, p_c]$
$K_c > 1-\epsilon$	$(s+K_i^*)/(s+\lambda)$	$\sim K_i^*/s \quad \omega \in [\lambda, K_i^*]$
$K_c = 1$	$(K_i^*+s)/s$	$\sim K_i^*/s \quad \omega \in [0, K_i^*]$

2.1. Equivalent regulation

An equivalent regulation formulation of the hybrid I(N)DI control law from Fig. 1 can be found by closing the input feedback path. This yields:

$$u(s) = C_c(s)\hat{\mathcal{B}}^{-1}\left(\nu(s) - \left[1 - K_c H_c(s)\right]\hat{\mathcal{A}}\hat{x}(s) - \left[K_c H_c(s) G(s)\right]\dot{y}_{CV}(s)\right) \tag{8}$$

where $C_c(s) \triangleq (1 - K_c H_c(s))^{-1}$. In order to make the concept of equivalent regulation more tangible, it is useful to decompose the compensation dynamics $C_c(s) \triangleq C_c^*(s)H_c^*(s)$ into a combination of first-order lag-lead *regulation* contribution C_c^* and a high-order filter H_c^* with unity DC-gain:

$$C_c^*(s) = \frac{s + z_c}{s + p_c} \tag{9}$$

$$H_c^*(s) = \frac{C_c(s)}{C_c^*(s)} \tag{10}$$

A case-by-case overview of C_c^* is provided in Table 1 for different values of K_c. The third column shows that this regulation contribution term adds additional gain at low frequencies, which can range from small refinements to full integral action. In this light, another important observation is that Equation (8) is *equivalent* to:

$$\begin{aligned}u(s) &= \hat{\mathcal{B}}^{-1}\left(C_c^*(s)H_c^*(s)\left[\nu(s) - sK_c H_c(s)G(s)y_{CV}(s)\right] - \hat{\mathcal{A}}\hat{x}(s)\right) \\ &\triangleq \hat{\mathcal{B}}^{-1}\left(\nu^*(s) - \hat{\mathcal{A}}\hat{x}(s)\right)\end{aligned} \tag{11}$$

Hence, taking a two-degree-of-freedom virtual control design according to

$$\nu(s) = C_{OL}(s)\begin{bmatrix} r(s) & y_{CV}(s)\end{bmatrix}^T = F_{OL}(s)r(s) - K_{OL}(s)y_{CV}(s) \tag{12}$$

one finds:

$$\nu^*(s) = C_c^*(s)H_c^*(s)\left[F_{OL}(s)r(s) - \left[K_{OL}(s) + sK_c H_c(s)G(s)\right]y_{CV}(s)\right] \tag{13}$$

This shows that the hybrid I(N)DI strategy effectively boils down to a *model-based* (N)DI control law with a more advanced virtual control design. Next to the equivalent regulation term $C_c^*(s)$, this equivalent vir-

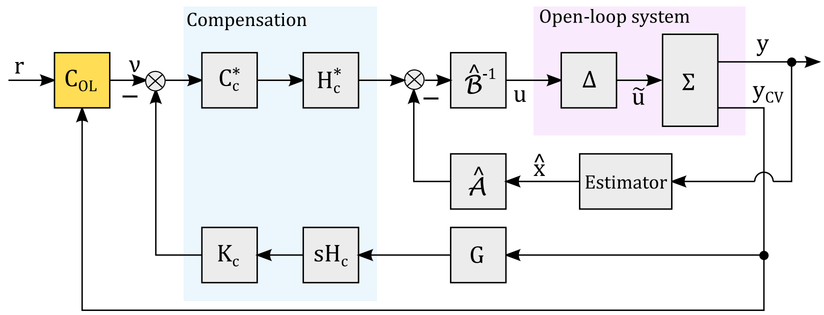

Fig. 2. Hybrid I(N)DI equivalent regulation formulation.

tual control contains additional high-pass (derivative) action induced by $sK_cH_c(s)G(s)$. With this formulation, a hybrid INDI control law can be thought of in terms of equivalent virtual control loop shaping considerations as if it were a purely model-based NDI design. Fig. 2 visualizes this.

The equivalent regulation concept provides a good understanding of the effect of inversion error compensation in hybrid INDI. Still, it may not be immediately obvious that the high-order elements H_c^* and G introduce dynamic artifacts that may threaten stability if not considered appropriately. The design of the compensation filter H_c is again critical here. This concerns the principle of *synchronization*, as discussed next.

2.2. Synchronization principle

From this discussion, it follows that a key objective in INDI-based control design is to achieve a robustly stable or *balanced* combination of equivalent regulation terms, high-order filter H_c^*, and additional dynamics G and Δ. Some basic design principles apply to mitigate the detrimental impact of these additional dynamics on stability, which is also known as the *synchronization effect* [42]. This effect typically manifests itself as an additional high-frequency oscillation on top of the anticipated control signal in sensor-based inversion designs [44,45]. As mentioned before, the term ‘synchronization’ refers to the relative timing or phase between the sensor-based estimate of the output derivative and the input feedback signal. This terminology is maintained here; however, a more complete interpretation is that the effect originates from a difference between direct feedthrough terms. This is illustrated in Fig. 3, which shows the components associated with the sensor-based part of the inversion loop in isolated and reorganized form. This representation allows for a more focused view on the synchronization effect.

Robust stability of the isolated system from Fig. 3 implies that the feedback interconnection remains well-posed for all $\Delta \in \boldsymbol{\Delta}$. This requires the following system to have a causal inverse:

$$I + K_c H_c \left[K_{\mathcal{B}} G \Delta (P + I) - I \right] \triangleq I + L_s \tag{14}$$

where $K_{\mathcal{B}} \triangleq \hat{\mathcal{B}}^{-1}\mathcal{B}$. Consequently, the *synchronization sensitivity* transfer function $S_s(s) \triangleq (I + L_s(s))^{-1} = e(s)/\nu(s)$ must exist as a member of real rational transfer function matrices. One can interpret S_s as a direct indication of the sensor-based inversion error; therefore, it represents a useful instrument to assess inversion quality. However, these insights are obtained based on a location that is effectively embedded in the control law itself. Consequently, S_s offers insufficient insight into the robustness and disturbance rejection performance at the level of the plant. To get a complete picture of the synchronization effect, the plant input sensitivity function $S_i(s) = u(s)/d_i(s)$ must be considered as well:

$$\left(I + K_c H_c C_c K_{\mathcal{B}} G \Delta (P + I) \right)^{-1} \triangleq \left(I + L_i \right)^{-1} \triangleq S_i = (1 - K_c H_c) S_s \tag{15}$$

The last equality directly reflects the equivalent regulation effect of inversion error compensation; for example, high-pass filter action emerges when $K_c = 1$ and H_c is strictly proper.

To simplify the upcoming analysis, the low-frequency plant contribution described by P is disregarded. This is justified based on the understanding that the synchronization effect generally manifests itself in the high-frequency spectrum, as G and Δ typically operate on relatively fast time scales. Accordingly, it appears reasonable to insist on well-posedness of Equation (14) when $P = 0$. Based on this simplification, the following H_∞ synchronization design principle can be defined: given K_c,

$$\begin{aligned} \min \quad & \|S_s\|_\infty = \left\| \left(I + K_c H_c \left[G K_{\mathcal{B}} \Delta - I \right] \right)^{-1} \right\|_\infty, \quad \text{while} \\ & \|S_i\|_\infty = \left\| \left(I + K_c H_c C_c G K_{\mathcal{B}} \Delta \right)^{-1} \right\|_\infty = M_i \end{aligned} \tag{16}$$

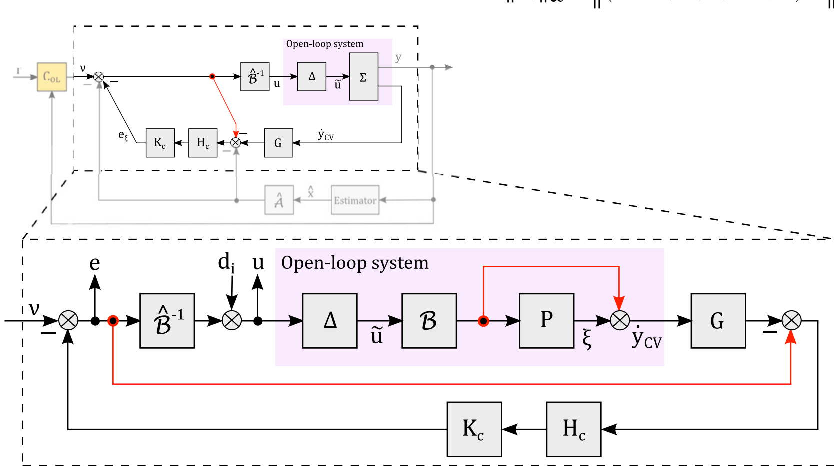

Fig. 3. Isolated sensor-based inversion elements in re-organized form; the concept of synchronization is highlighted in red and is due to a difference in direct feedthrough terms. (For interpretation of the colors in the figure(s), the reader is referred to the web version of this article.)

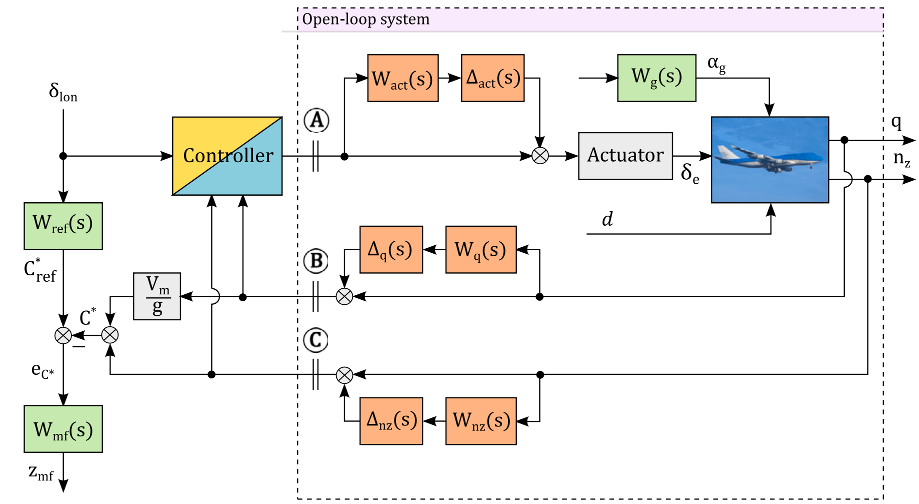

Fig. 4. Control system interconnection structure.

Here, M_i represents an upper bound on the input sensitivity function that is specified by the designer. The peak magnitude of the plant input sensitivity function $\|S_i\|_\infty$ has a close relation to broken-loop stability margins; for example, an upper bound $M_i = 2$ corresponds to a disk-based gain and phase margin of at least 6 dB and 29 degrees, respectively [46]. Note that if $\|S_i\|_\infty > 1$, equivalent regulation is ensured in terms of finite disturbance rejection action according to Bode's sensitivity integral theorem [46]. Accordingly, the above H_∞ synchronization design principle maximizes inversion quality while achieving finite feedback performance within a stability margin limit set by the designer. This can be used as a guideline to select an effective inversion error compensation filter structure.

3. Design case study

This section introduces the case study that serves as the basis for the remainder of this paper. An overview of the (controller-agnostic) system interconnection structure under consideration is presented in Fig. 4. This structure applies to both PID and hybrid INDI designs. A description of the flight control system model used for synthesis and analysis is provided in Subsection 3.1. The design requirements that are to be met by the control laws are described in Section 3.2.

3.1. Flight control system model

A brief background on the nonlinear airframe model database and its linearization is provided first. This is followed by a description of the control system hardware and the system uncertainty model.

3.1.1. Boeing 747-100/200 GARTEUR RECOVER airframe model

The Boeing 747-100/200 RECOVER Simulation Benchmark Version 3.0 software[3] developed by the GARTEUR Flight Mechanics Action Group FM-AG16 [50,51] is adopted as the rigid-body flight dynamics model in this work. The simulation is built on MATLAB/Simulink® and the Delft University's Aircraft Simulation and Analysis Tool (DASMAT) environment [52] and is based on data prepared by The Boeing Company for the NASA Ames Research Center [53,54]. The airframe model is trimmed and linearized around selected operating conditions. In this work, the scope is limited to the short-period mode only. This leads to the following nominal system family:

$$\begin{bmatrix} \dot{\alpha} \\ \dot{q} \end{bmatrix} = \begin{bmatrix} Z_\alpha(\rho) & 1 \\ M_\alpha(\rho) & M_q(\rho) \end{bmatrix} \begin{bmatrix} \alpha \\ q \end{bmatrix} + \begin{bmatrix} 0 \\ M_{\delta_e}(\rho) \end{bmatrix} \delta_e - \begin{bmatrix} Z_\alpha(\rho) \\ M_\alpha(\rho) \end{bmatrix} \alpha_g \tag{17}$$

The nominal dynamics are extended with uncertainty and an additional disturbance term to address model variations and imperfections. This results in the following system formulation:

$$\begin{bmatrix} \dot{\alpha}(t) \\ \dot{q}(t) \end{bmatrix} = \begin{bmatrix} \left(1 + W_{Z_\alpha}\bar{\delta}_{Z_\alpha}\right) Z_\alpha(\rho) & 1 \\ \left(1 + W_{M_\alpha}\bar{\delta}_{M_\alpha}(t)\right) M_\alpha(\rho) & \left(1 + W_{M_q}\bar{\delta}_{M_q}(t)\right) M_q(\rho) \end{bmatrix} \begin{bmatrix} \alpha(t) \\ q(t) \end{bmatrix} + \begin{bmatrix} 0 \\ \left(1 + W_{M_{\delta_e}}\bar{\delta}_{M_{\delta_e}}(t)\right) M_{\delta_e}(\rho) \end{bmatrix} \left(1 + W_{act}\bar{\Delta}_{act}\right) \delta_e(t) - \begin{bmatrix} Z_\alpha(\rho) \\ M_\alpha(\rho) \end{bmatrix} \alpha_g(t) + \begin{bmatrix} W_Z \\ W_M \end{bmatrix} d(t) \tag{18}$$

Here, $\bar{\delta}_\bullet \in [-1, 1]$ and $\|\bar{\Delta}_\bullet(j\omega)\|_\infty \leq 1$ represent normalized real (parametric) and complex (dynamic) uncertainty, respectively; $W_\bullet(s)$ represents an uncertainty weight, and is discussed in greater detail shortly. The scheduling vector $\rho = \begin{bmatrix} h & M \end{bmatrix}^T$ consists of altitude h and Mach number M. Atmospheric disturbance is introduced according to $\alpha_g = W_g \bar{\alpha}_g$, with $|\bar{\alpha}_g| \leq 1$, with W_g describing intensity; other disturbances are lumped into d. The time-varying nature of some variables has been made explicit in anticipation of Subsection 3.1.3. The output equation describes the accelerometer and rate gyro sensor measurements according to:

$$\begin{bmatrix} q_m(t) \\ n_{z_m}(t) \end{bmatrix} = \begin{bmatrix} \left(1 + W_q\bar{\Delta}_q\right) & 0 \\ 0 & \left(1 + W_{n_z}\bar{\Delta}_{n_z}\right) \end{bmatrix} \cdot \begin{bmatrix} 0 & 1 \\ -\frac{V_0(\rho)}{g}\left(1 + W_{Z_\alpha}\bar{\delta}_{Z_\alpha}\right) Z_\alpha(\rho) & 0 \end{bmatrix} \begin{bmatrix} \alpha(t) \\ q(t) \end{bmatrix} \tag{19}$$

Here, $n_z = -V_0/g Z_\alpha \alpha$ with V_0 representing the reference trim speed and g the gravitational acceleration. This output model represents a scenario where the sensors pick up additional, unmodeled dynamics.

3.1.2. Flight control system (FCS) hardware model

The control system model incorporates actuator dynamics and digital artefacts associated with the flight control computer. The RECOVER library includes a complete model description of the actuator travel limitations of the hydro-mechanical flight control system. However, a model of the dynamic response characteristics is not available. Therefore, use will be made of a simple second-order LTI system representation for the elevator dynamics [55]:

[3] The GARTEUR RECOVER Benchmark is licensed under an Open Software License (OSL) 3.0; details on how the software package can be accessed can be found on http://www.faulttolerantcontrol.nl/.

$$G_{act}(s) = \frac{\omega_{n_{act}}^2}{s^2 + 2\zeta_{act}\omega_{n_{act}} s + \omega_{n_{act}}^2} \tag{20}$$

where $\zeta_{act} = 0.7$ and $\omega_{n_{act}} = 20$ rad/s. This corresponds to an elevator bandwidth that is typical for a large transport aircraft [56]. The travel and rate limits correspond to $[-17, +23]$ degrees and ± 37 deg/s, respectively.

Digital control effects are incorporated based on the modified continuous design approach [57]. It is assumed that the flight control computer (FLCC) runs at a sampling rate of 80 Hz, which is in agreement with existing design studies [58]. The following approximations are used for the zero-order hold (ZOH), computational delay, and anti-aliasing filter:

$$G_{ZOH}(s) = \frac{1 - e^{-T_s s}}{sT_s}, \quad G_{del}(s) = e^{-T_s s}, \quad G_{alias}(s) = \frac{150}{s + 150} \tag{21}$$

Here, T_s represents the sampling time. First-order Padé approximations are used for $-e^{-T_s s}$. The anti-aliasing filter is configured well below the Nyquist frequency [57]. Finally, ideal sensor dynamics are assumed.

3.1.3. Uncertainty model

Table 2 provides a summary of the selected parametric (scalar) uncertainty and disturbance bounds. The absolute uncertainty bounds were determined based on qualitative insights regarding weight and balance variations and typical aerodynamic uncertainties associated with transport aircraft. The moment coefficients are considered arbitrarily fast time-varying. Clearly, this scenario is very conservative; however, it provides an upper bound on linear time-varying (LTV) response behavior. The disturbance bounds reflect moderate gust levels and other exogenous effects due to e.g. airframe configuration changes.

Fig. 5 visualizes the dynamic uncertainty shaping filters $W_\bullet(s)$, which are defined as individual transfer functions. These reflect a scenario where measurements are contaminated by uncertain flexible airframe modes and the actuator dynamics deviate from their assumed second-order behavior in the high-frequency region. Notably, the presented weights imply that the phase relation is lost beyond a particular frequency (i.e., the frequency where the uncertainty magnitude exceeds 0 dB). This loss of phase information is typical for physical systems [59,46] and demands gain stabilization.

As an example, Fig. 6 visualizes the sensor output frequency spectra corresponding to the uncertainty sample $\bar{\Delta}_\bullet = 1$. This illustrates how resonance peaks take form in the high-frequency region. These can be recognized as measurement corruptions induced by flexible modes, as seen in e.g. [59].

3.2. Design requirements

The design requirements fall into a number of categories. A background on flying qualities is provided first, which relates to the soft design objective. These must be optimized within limitations imposed by hard requirements, which are discussed secondly. These consist of nominal model matching performance, control activity, and stability margins.

3.2.1. Flying qualities

The design objective is to generate a desired C^*-to-stick response and minimize deviations in the presence of uncertainty and disturbance. The C^* output at the instantaneous center of rotation (ICR) is defined as:

Table 2
Parametric uncertainty and disturbance model overview.

Uncertainty bounds				Disturbance bounds		
Variable	Unit	Absolute	Rate	Variable	Unit	Absolute
W_{Z_α}	[−]	±10%	0	W_Z	[g]	0.25
W_{M_α}	[−]	±50%	±∞	W_M	[deg/s^2]	3.0
W_{M_q}	[−]	±30%	±∞	W_g	[deg]	2.0
$W_{M_{\delta_e}}$	[−]	±20%	±∞			

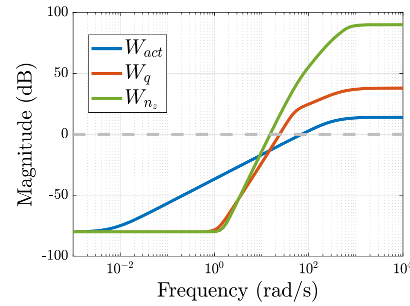

Fig. 5. Dynamic uncertainty weight profiles.

$$C^* = n_{z_{ICR}} + \frac{V_m}{g} q = -Z_\alpha \frac{V_0}{g}\alpha + \frac{V_m}{g} q \tag{22}$$

Here, V_m represents the cross-over velocity; $V_m/g = 12.4$ is generally selected [57]. The desired dynamics for the C^*-to-stick response are established based on recommendations specified in [60,61]:

$$\frac{C^*_{des}(s)}{r(s)} = \frac{K_{des}(s + z_{des})}{s^2 + 2\zeta_{des}\omega_{des} s + \omega_{des}^2} \tag{23}$$

where r represents the pilot stick input signal. To minimize control activity, the desired modal characteristics are selected in close accordance with the nominal bare airframe dynamics in standard conditions. This is in agreement with industry practice [62]. The attitude and flight path bandwidth criteria are used in combination with Gibson's dropback criterion [61] to obtain desired values for the short-period frequency, damping, and C^* numerator time constants. These are summarized in Table 3. The selected desired dynamics correspond to predicted Level-1 performance for Class III aircraft (heavy transport) and Category B flight phase [60] in cruise; in the approach condition, the specifications enter the region of Level-2 performance.

3.2.2. Nominal and robust performance objectives

The degree of compliance with the desired flying qualities is quantified in terms of an H_∞ model-following error. A distinction is made between the nominal and uncertain system in terms of permissible error bound. Enforcing a tighter bound on the nominal system case ensures the system behaves as intended in the presence of known high-order dynamics, while the remaining design margin is used to improve robustness. This approach favors average flying quality performance over remote worst-case scenarios. This leads to the following definition of the model-following performance metric:

$$z_{mf}(s) = W_{nom} W_{mf}(s)\left[C^*_{des}(s) - C^*(s)\right] \tag{24}$$

Here, $W_{mf}(s)$ represents a first-order low-pass filter that scales the model-following error as a function of frequency in the uncertain case:

$$W_{mf}(s) = \frac{2}{s + 0.01} \tag{25}$$

This reflects the frequency range that is of interest to the human pilot. In the nominal scenario, an additional constant factor $W_{nom} = 15$ is added. The nominal performance objective is enforced as a hard requirement, whereas the robust performance criterion serves as the soft design objective.

3.2.3. Control activity and stability constraints

To prevent the onset of pilot induced oscillations (PIOs) and minimize actuator wear, actuator rate and travel limits must be avoided

Table 3
Desired short-period mode characteristics (flaps up, 317 ton, XCG 25%).

Phase	Condition (M, h, $\bar{q}$)	ω_{des} [rad/s]	ζ_{des} [-]	z_{des} [1/s]
Cruise	0.85, 30 kft, 15 kPa	1.3	0.8	1.5
Approach	0.38, 5 kft, 8.5 kPa	0.9	0.8	1.1

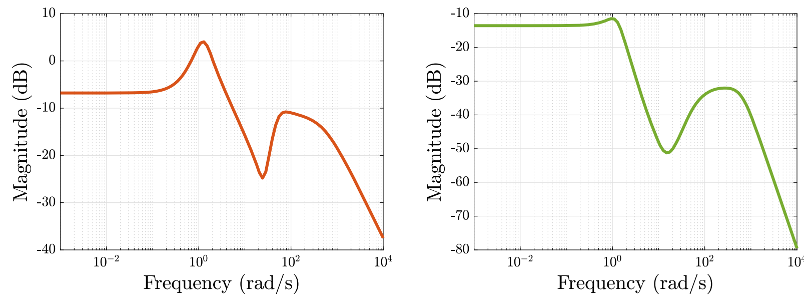

(a) Elevator to q sensor path (b) Elevator to n_z sensor path

Fig. 6. Example sensor signal profiles.

as much as possible. Mitigation of actuator limits for pilot stick inputs is therefore enforced as a hard requirement. Other design constraints relate to stability margins at the airframe input (elevator) and output (pitch rate and vertical acceleration sensors). Specifically, a disk margin specification corresponding to +6dB upper gain margin (GM) and 36.87 degrees phase margin (PM) is imposed based on the elliptical disk exclusion region framework from [9]. This requirement is enforced in the presence of real and complex uncertainty at all locations. This is relatively conservative [9] and can be compared to an early design scenario where additional margins are required [63].

4. Control law architectures

With this background in place, the gain-scheduled PID and hybrid INDI control architectures of interest are introduced in this section. A preliminary design procedure based on low-order analytical pole placement is described for both methods. These preliminary design insights serve as a basis for formal synthesis in the subsequent sections. The two-degree-of-freedom gain-scheduled PID structure is presented first. Then, two hybrid INDI architectures are considered. First, a rate inversion design is presented which has direct commonality to the gain-scheduled PID control law. Second, a modular C^*-inversion design is described which leverages visible design decoupling in terms of flying qualities, robustness, and gain scheduling. The inversion error compensation filter architecture is elaborated upon as well, based on the synchronization guidelines from Section 2.2. The section concludes with an overview of design parameters.

4.1. Gain-scheduled proportional-integral-derivative (PID) architecture

A baseline C^* two-degree-of-freedom (2DOF) proportional-integral (PI) control architecture is described in [55]. The basis of this architecture is seen in many classical flight control law designs [2,4,22]. A pitch acceleration term is added as a derivative (D) term to this baseline structure. This ensures close commonality with the hybrid INDI control design presented in the subsequent section. Note that similar incorporation of angular acceleration feedback saw application in the experimental X-29 aircraft [64]. Consequently, the PID control law takes the following form:

$$u = K_f \tilde{r} + \frac{K_i}{s}\left(\tilde{r} - C^*\right) - K_p C^* - K_q q - K_{\dot{q}}\dot{q} \tag{26}$$

A first-order pre-filter is used as an additional design degree-of-freedom to achieve desired handling qualities [65,55]:

$$\tilde{r} = \left(\frac{\tau_p^n s + 1}{\tau_p^d s + 1}\right) r \tag{27}$$

A block diagram visualization is shown in Fig. 7. A standard pole-zero placement procedure to obtain the design parameters is described by [55]. However, the additional pitch acceleration feedback signal

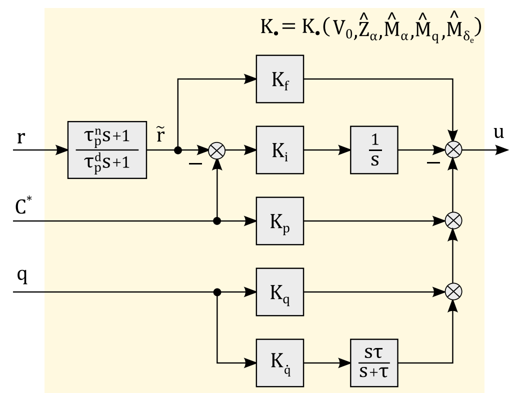

Fig. 7. Gain-scheduled Proportional-Integral-Derivative (PID) control law structure.

makes Equation (26) redundant from a low-order, nominal pole placement perspective. This can be shown by treating the derivative gain $K_{\dot{q}}$ as a known variable and closing the angular acceleration loop. In doing so, the following equivalent expression is found for the remaining gains:

$$u = \tilde{K}_f r + \frac{\tilde{K}_i}{s}\left(r - C^*\right) - \tilde{K}_p C^* - \tilde{K}_q q \tag{28}$$

where:

$$\begin{aligned}
&\tilde{K}_f \triangleq \tilde{K}_{\dot{q}} K_f, \quad \tilde{K}_i \triangleq \tilde{K}_{\dot{q}} K_i,\\
&\tilde{K}_p \triangleq \tilde{K}_{\dot{q}}\left[K_p - K_{\dot{q}} Z_\alpha^{-1} M_\alpha \left(\frac{V_0}{g}\right)^{-1}\right],\\
&\tilde{K}_q \triangleq \tilde{K}_{\dot{q}}\left[K_q + K_{\dot{q}} Z_\alpha^{-1} M_\alpha \left(\frac{V_m}{V_0}\right) + K_{\dot{q}} M_q\right],\\
&\tilde{K}_{\dot{q}} \triangleq (1 + K_{\dot{q}} M_{\delta_e})^{-1}
\end{aligned} \tag{29}$$

These equivalent gains indicate that the effect of pitch acceleration feedback can be offset in all cases. From here, the equivalent feedback and feedforward gains can be determined through the analytical pole-zero placement procedure. Firstly, the closed-loop transfer function is expressed as a function of the controller gains:

$$\frac{C^*(s)}{r(s)} = \frac{s^2 b_1 \tilde{K}_f + s(b_0 \tilde{K}_f + b_1 \tilde{K}_i) + b_0 \tilde{K}_i}{s^3 + s^2(a_1 + M_{\delta_e}\tilde{K}_q + b_1 \tilde{K}_p) + s(a_0 - Z_\alpha M_{\delta_e}\tilde{K}_q + b_0 \tilde{K}_p + b_1 \tilde{K}_i) + b_0 \tilde{K}_i} \tag{30}$$

where

$$\begin{aligned}
&a_0 = Z_\alpha M_q - M_\alpha, \quad a_1 = -Z_\alpha - M_q,\\
&b_0 = -\frac{M_{\delta_e} Z_\alpha}{g}(V_0 + V_m), \quad b_1 = M_{\delta_e}\frac{V_m}{g}
\end{aligned} \tag{31}$$

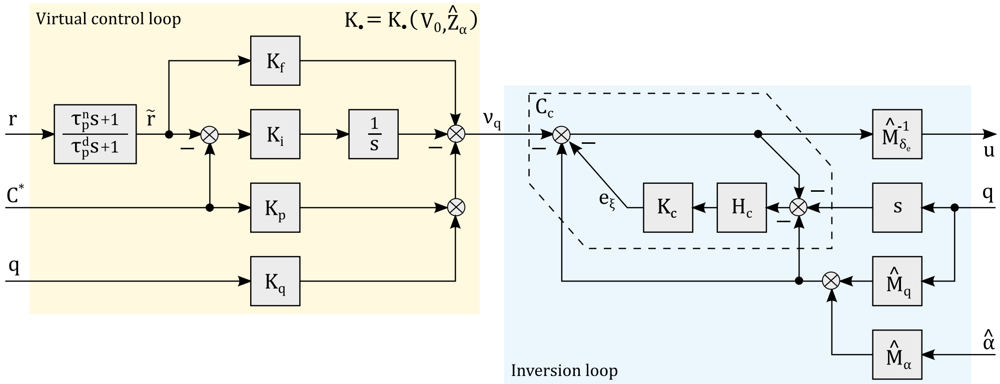

Fig. 8. Hybrid INDI (rate inversion) control law.

Secondly, the *target* desired dynamics described by Equation (23) are augmented by an additional pole and zero as follows [55]:

$$\frac{C^*_{des}(s)}{r(s)} = \frac{p_3\omega^2_{des}}{z_2 z_{des}} \frac{(s+z_2)(s+z_{des})}{(s+p_3)\left(s^2+2\zeta_{des}\omega_{des}s+\omega^2_{des}\right)} \tag{32}$$

Consequently, the design parameters can be written directly in terms of the desired dynamics and the airframe stability and control coefficients. The low-order desired dynamics can be restored by selecting $z_2 = p_3$, which eliminates the integrator mode from the piloted response. Therefore, implicit model-matching (model-following) is achieved through adequate selection of feedforward and feedback gains. To further improve flying qualities, the remaining zero can be set through prefilter pole-zero cancellation [55]:

$$\tilde{r} = \left(\frac{z_{des}s+1}{b_0/b_1 s+1}\right) r \tag{33}$$

Finally, gain scheduling is to be performed based on an on-board model (OBM) representation of the nominal short-period dynamics described by Equation (17) [55,5]. This is also indicated in Fig. 7. As demonstrated in [66], the procedure naturally translates to nonlinear implementations based on velocity-based scheduling [14,15] to prevent hidden couplings.

4.2. Equivalent hybrid INDI architecture (rate inversion)

The gain-scheduled PID control law from the previous section can be *equivalently* formulated as a gain-scheduled hybrid IDI (i.e., INDI) control law with pitch rate as the inversion pitch-axis command variable (MCV) and a C^* outer-loop regulator. The moment dynamics form the point of departure for the derivation:

$$\dot{q} = M_\alpha\alpha + M_q q + M_{\delta_e}\delta_e \tag{34}$$

The inversion loop is constructed to generate a nominal closed-loop inversion response according to $q(s)/\nu_q(s) = 1/s$, with ν_q representing the outer loop (virtual) control input variable. Writing ξ to represent the non-input related terms as in Equation (5), the inversion control law can be expressed in generic form as:

$$u = M^{-1}_{\delta_e}\left(\nu_q - \hat{\xi}\right) \tag{35}$$

The selected PI virtual control law structure is similar to Equation (28):

$$\nu_q = K_f r + \frac{K_i}{s}\left(r - C^*\right) - K_p C^* - K_q q \tag{36}$$

Consequently, a pole placement design strategy can be established based on the closed-loop inversion response and the following relationships:

$$\frac{\alpha(s)}{q(s)} = \frac{1}{s-Z_\alpha}, \quad \frac{C^*(s)}{q(s)} = \frac{n_z(s)}{q(s)} + \frac{V_m}{g} = -Z_\alpha\frac{V_0}{g}\frac{\alpha(s)}{q(s)} + \frac{V_m}{g} \tag{37}$$

As a result, the full closed-loop stick input response can be written as:

$$\frac{C^*(s)}{r(s)} = \frac{s^2 b_1 K_f + s(b_0K_f + b_1K_i) + b_0K_i}{s^3 + s^2(-Z_\alpha + K_q + b_1K_p) + s(-Z_\alpha K_q + b_0K_p + b_1K_i) + b_0K_i} \tag{38}$$

where

$$b_0 = -\frac{Z_\alpha}{g}(V_0+V_m), \quad b_1 = \frac{V_m}{g} \tag{39}$$

The similarities between these expressions and Equations (30) and (31) become apparent by considering an equivalent PID formulation. In the low-order design case ($K_c < 1$, $H_c = 1$), the following equivalent gains apply:

$$\begin{aligned} &\tilde{K}_f = M^{-1}_{\delta_e}C_cK_f, \quad \tilde{K}_i = M^{-1}_{\delta_e}C_cK_i, \quad \tilde{K}_{\dot{q}} = M^{-1}_{\delta_e}C_cK_c, \\ &\tilde{K}_p = M^{-1}_{\delta_e}C_cK_p - M^{-1}_{\delta_e}Z^{-1}_\alpha M_\alpha\left(\frac{V_0}{g}\right)^{-1}, \\ &\tilde{K}_q = M^{-1}_{\delta_e}C_cK_q + M^{-1}_{\delta_e}Z^{-1}_\alpha M_\alpha\frac{V_m}{V_0} + M^{-1}_{\delta_e}M_q \end{aligned} \tag{40}$$

Here, $C_c = (1-K_c)^{-1}$ according to Section 2.1. Substituting the control gains obtained from Equation (38) and comparing the result to Equations (29)-(31) shows that both pole placement strategies are *equivalent*. The moment terms are all cancelled by dynamic inversion, which leaves V_0 and Z_α as the only airframe dependencies that require gain scheduling of the outer loop. In case the inversion loop collapses to a model-based strategy ($K_c = 0$), the control law can be shown to be equivalent to the proportional-integral (PI) baseline from Section 4.1. However, as discussed before in Section 2, the incorporation of dynamics in H_c leads to additional feedback action and possibly high-order dynamics. Given the fact that inversion error compensation may lead to complete integral action (see Table 1), there therefore exists a degree of duplicate functionality in combination with the outer-loop integral path. This commonality is exploited in [66].

4.3. Modular hybrid INDI architecture (C^* inversion)

As discussed before, an important aspect of the (I)NDI design philosophy is the visible decoupling of design goals within the control law architecture itself. Such a modular approach to flight control law design is beneficial for a number of reasons: for example, it results in a high degree of design visibility, which aids the verification process [13]. Moreover, the design structure can be efficiently transferred across different airframes [25]. This is in contrast to the PI(D) design from Fig. 7

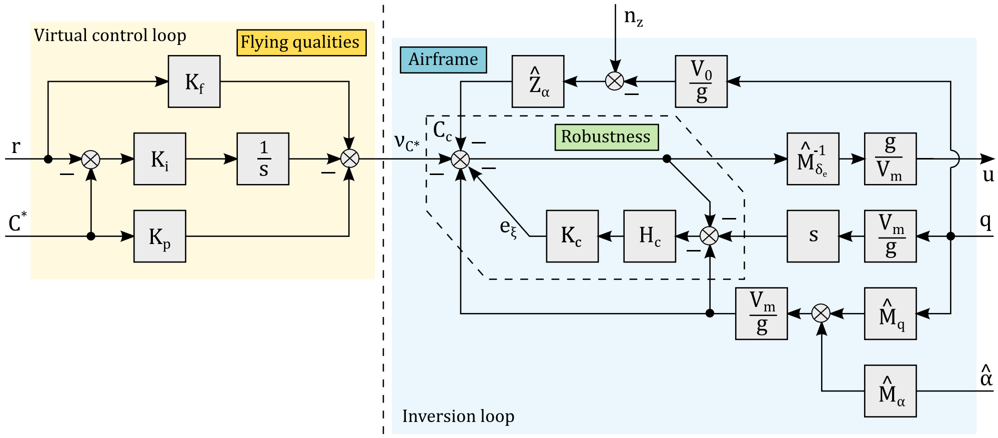

Fig. 9. Hybrid INDI (C^* inversion); the visible decoupling of design goals (desired flying qualities, robustness) from the bare airframe dynamics results in a modular structure.

and - to a lesser extent - the outer loop structure in Fig. 8, where all functionalities collapse into a combination of gains.[4]

The concept of hybrid INDI enables the incorporation of a separate design module to improve robustness in the context of implicit model-following (IMF) NDI design. This is achieved using the concept of inversion error compensation from Section 2. As opposed to the configuration discussed before, the outer loop is set up based on desired flying qualities only in this case. Gain scheduling and robustness is then achieved in the inversion loop. This decoupling of design goals is indicated in the block diagram structure[5] in Fig. 9. To derive the control law, the nominal equations of motion are used:

$$\begin{bmatrix} \dot{\alpha} \\ \dot{q} \end{bmatrix} = \begin{bmatrix} Z_\alpha & 1 \\ M_\alpha & M_q \end{bmatrix} \begin{bmatrix} \alpha \\ q \end{bmatrix} + \begin{bmatrix} 0 \\ M_{\delta_e} \end{bmatrix} \delta_e \tag{41}$$

Writing the command variable as $y_{CV} = C^* = n_z + \frac{V_m}{g} q$ and taking its time derivative according to the standard NDI (feedback linearization) design procedure [67] leads to the following expression of the output dynamics:

$$\dot{y}_{CV} = \dot{n}_z + \frac{V_m}{g}\dot{q} = -Z_\alpha \frac{V_0}{g}\dot{\alpha} + \frac{V_m}{g}\dot{q} \tag{42}$$

The first term can be reformulated using the nominal force equation:

$$-Z_\alpha \frac{V_0}{g}\dot{\alpha} = -Z_\alpha \frac{V_0}{g}\left(Z_\alpha \alpha + q\right) = Z_\alpha \left(n_z - \frac{V_0}{g} q\right) \tag{43}$$

Therefore, the C^* output dynamics can be rewritten as:

$$\dot{y}_{CV} = Z_\alpha \left[n_z - \frac{V_0}{g} q\right] + \frac{V_m}{g}\dot{q} \tag{44}$$

Based on Equation (41), the control input u ($= \delta_e$) appears directly through the $\dot{q}$ term. Writing the moment equation once again as $\dot{q} = \xi + M_{\delta_e} u$ and re-arranging terms results in the following dynamic inversion control law:

$$u = \left(\frac{M_{\delta_e} V_m}{g}\right)^{-1} \left(\nu_{C^*} - Z_\alpha \left[n_z - \frac{V_0}{g} q\right] - \frac{V_m}{g}\hat{\xi}\right) \tag{45}$$

For the virtual control loop, the following design is selected:

$$\nu_{C^*} = K_f r + \frac{K_i}{s}\left[r - C^*\right] - K_p C^* \tag{46}$$

This choice results in the following stick response in the case of ideal inversion, irrespective of the bare airframe dynamics:

$$\frac{C^*(s)}{r(s)} = \frac{K_f s + K_i}{s^2 + K_p s + K_i} \tag{47}$$

The resulting transfer function has precisely the form of the desired C^*-to-stick response from Equation (23). To achieve implicit model-matching (model-following), the desired flying qualities directly map to the outer loop gains. Therefore, the effect on robustness of the outer loop cannot be influenced without changing pilot handling behavior. The inversion error compensation loop serves as an additional design degree-of-freedom in this context. This requires the setup of an appropriate augmentation structure, as discussed next.

4.4. Compensation filter structure

As discussed in Section 2.2, managing the impact of high-order dynamics and uncertainty is an important element of INDI-based control design. To this end, the H_∞ synchronization design principle is applied in this section to establish an appropriate compensation filter structure for the presented hybrid INDI architectures. In the present case, the synchronization sensitivity function takes the following form:

$$S_s(s) = \left(I + K_c H_c(s)\left(G(s)\Gamma_\Delta(s) - I\right)\right)^{-1} \tag{48}$$

Here, G includes all nominal dynamics that are not 'synchronized'. The plant input sensitivity function S_i is similarly defined. The uncertainty terms are captured by Γ_Δ according to

$$\Gamma_\Delta(s) \triangleq K_B(I + W_{act}(s)\Delta_{act}(s))(I + W_q(s)\Delta_q(s)) \tag{49}$$

A routine approach to inversion filter architecture selection is to 'synchronize' or *match* the perturbing dynamics on the angular acceleration and input feedback channels [43,37,42]. This process essentially boils down to deciding which parts of G get carried over (virtually) to the compensation filter H_c. Fig. 10 illustrates the main idea behind concept.

Several candidate design architectures are listed in Table 4. Candidate #4 represents a special case in the sense that all perturbing dynam-

Table 4
Compensation filter candidates H_c in the context of synchronization.

#ID	Synchronous part (H_c)	Asynchronous part (G)
1	1	$G_{del}G_{ZOH}G_{act}G_{alias}H_d$
2	H_d	$G_{del}G_{ZOH}G_{act}G_{alias}$
3	$G_{act}H_d$	$G_{del}G_{ZOH}G_{alias}$
4	$G_{del}G_{ZOH}G_{act}G_{alias}H_d$	1

[4] However, the functional transparency and flexibility can be restored for this type of control structure by an online pole placement strategy as presented in [4,5].

[5] Similar structures are presented in [38,39,25].

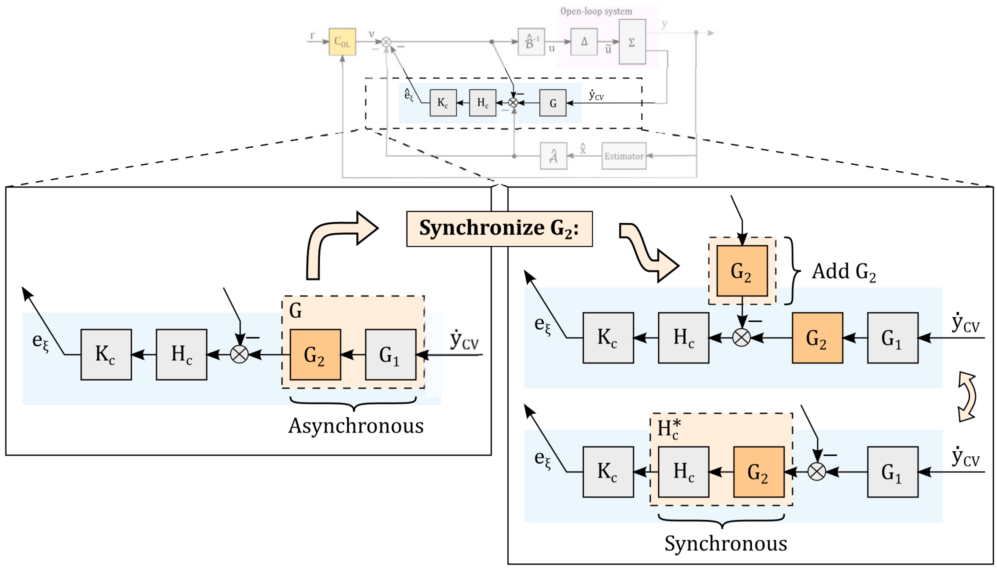

Fig. 10. Compensation filter selection according to the synchronization principle.

Table 5
Effect of compensation filter H_c on sensitivity peak gains ($K_c = 0.5$, $M_i = 2.0$).

#ID	Sync. gain ($\|S_s\|_\infty$)		Input gain ($\|S_i\|_\infty$)	
	Nominal	Worst-case	Nominal	Worst-case
1	2.91	4.00	1.45	2.00
2	1.80	2.44	1.45	2.00
3	1.16	1.89	1.32	2.00
4	1.00	1.97	1.27	2.00

Table 6
Design parameter overview; 'X' denotes the parameter is available for optimization, whereas '-' implies it is not part of the design.

	Regulator					Derivative/Inversion	
Parameter	K_f	K_i	K_p	K_q	$K_{\dot{q}}$	K_c	$\tau \mid \tau_c$
Allowable range	free	free	free	free	free	[0.0-1.0]	[1.0-100]
PI	X	X	X	X	-	-	-
PID	X	X	X	X	X	-	X
INDI (q MCV)	X	X	X	X	-	X	X
INDI (C^* MCV)	X	X	X	-	-	X	X

ics G are synchronized. Using Equation (48), this implies that $S_s(s) = 1$ (perfect synchronization) in the absence of uncertainty. An overview of the effect of these different compensation filter architectures on the uncertain synchronization and plant input sensitivity functions is provided in Table 5. These have been established for a selected combination of compensation gain K_c and sensitivity bound M_i. The differentiator filter time constant is set such that the worst-case input sensitivity peak gain corresponds to the design value M_i. Therefore, all designs result in similar stability margins (in the isolated case, that is; see Fig. 3). The decreasing trend of the peak gain of S_s with filter complexity shows that inversion quality improves as more dynamics are synchronized. This shows the benefit of more elaborate filter architectures in the context of synchronization; however, the return gets increasingly small.

To maintain close commonality with the first-order derivative path of the PID design from Fig. 7, the first-order architecture corresponding to design #2 is selected. This option also improves inversion quality sufficiently, at little cost of complexity. Fig. 11 shows a block diagram illustration of how the first-order inversion architecture is implemented in a scaled complementary filter (SCF) setup as discussed in Section 2.

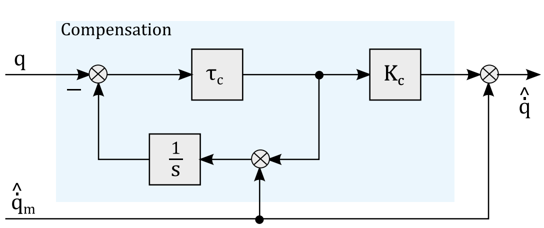

Fig. 11. First-order scaled complementary filter (SCF).

4.5. Design parameter overview

An overview of the design variables corresponding to each architecture is presented in Table 6. The implicit model-matching procedures outlined before are used to obtain preliminary values. Together with the acceleration gain, the proportional and integral feedback gains determine the location of the closed-loop short-period poles and the quickness of the integrator mode in the PID design. They are therefore all incorporated as free design parameters in the optimization. The feedforward gain K_f is kept as a free design parameter as well, although it could be obtained directly by performing pole-zero cancellation of the integrator mode instead. However, including K_f in the synthesis procedure improves model-following performance in the presence of high-order dynamics. The pre-filter settings follow directly from flying quality specifications and do not require robust optimization. They are therefore omitted from the overview in Table 6.

For the hybrid INDI designs, the inversion error compensation filter parameters are included in addition to the outer loop gains. This optimizes the inversion strategy itself. The permissible range of these constants is selected such that very slow or fast modes are prevented. All outer loop gains are included to improve model matching performance against the effects of high-order dynamics. Note that on-board model (OBM) selection represents another design degree-of-freedom that could be optimized [68,28]; however, this is not considered in this work. Instead, the nominal model information from Equation (17) is used.

5. Design optimization and robustness analysis

The combination of multi-objective design requirements and the uncertain and high-order nature of the control system requires the use of robust optimization to synthesize the design parameters. As discussed before, control law designs with guaranteed robust stability and perfor-

Algorithm 1: Multi-objective robust H_∞-synthesis routine for structured controllers against mixed uncertainty. More information about the listed subroutines can be found in Refs. [10,48,69–71].

Data: Soft and hard requirements, corresponding models P (performance) and P_N (Nichols disk margin), control law $K(p)$, initial design parameters p_0
Result: Locally optimal set of design parameters p^* and performance γ^*

Initialization Initialize $\hat{P}_\bullet = P_\bullet$ and $p = p_0$;
while *D-K termination conditions not met* **do**
  Non-smooth param. robust synthesis *K* step (MATLAB® `systune` [69,10,48,70])
  Optimize $\boldsymbol{p}$ over the entire set of scaled plants such that the set of hard requirements is robustly met and worst-case performance is maximized:

$$\min_{p\in\mathbb{R}^q} \gamma \quad \text{subject to:} \quad \max_{\delta\in\boldsymbol{\Delta}_p} \left\{ \left\| \hat{P}_\gamma(\delta) \star K(p) \right\|_\infty \right\} < 1, \tag{50}$$

$$\max_{\delta\in\boldsymbol{\Delta}_p} \left\{ \left\| \hat{P}_N^{(k)}(\delta) \star K(p) \right\|_\infty \right\} < 1 \quad \text{for all } k \in [1,\dots,M_N] \tag{51}$$

$$W_{nom} \cdot \left\| P_{(w,u)\to(z,y)}(0) \star K(p) \right\|_\infty < 1 \tag{52}$$

  Robustness against parametric uncertainties is achieved based on a dynamic inner approximation of the uncertainty set [48].
  Output: Optimal performance level γ^*, design parameters $\boldsymbol{p}^*$ corresponding to a locally H_∞-optimal structured controller, worst-case parametric uncertainty scenario set $\boldsymbol{\Delta}_{p,a}$;
  Frequency-wise D-scaling step (Using MATLAB® `ssv`)
  For every system $P_\bullet \in [P_{\gamma^*}, P_N]$, find $D^\bullet(j\omega)$ that minimizes over a finite frequency grid $\omega \in [\underline{\omega}, \dots, \overline{\omega}]$ the worst-case upper bound of the closed-loop system response in case of 1) the active parametric uncertainty scenario set $\boldsymbol{\Delta}_{p,a}$ and 2) dynamic uncertainty:

$$\min_{D\in D}\max_{\delta\in\boldsymbol{\Delta}_{p,a}} \bar{\sigma}\left(D_L^\bullet(P_\bullet(\delta) \star K(p^*)) \left(D_R^\bullet\right)^{-1}(j\omega) \right) \tag{53}$$

  Output: Optimal D-scalings as a function of frequency ω;
  Dynamic D-fitting step (Using MATLAB® `fitmagfrd` [71])
  Based on the magnitude for each $D^\bullet(j\omega)$, fit a minimum-phase transfer function $\hat{D}^\bullet(s)$; the result is used to scale all systems accordingly:

$$\begin{aligned}\hat{P}_\gamma = \operatorname{diag}&\left(\operatorname{diag}\left(0I_{1\times1}, I_{n_q\times n_q}, \frac{1}{\sqrt{\gamma}} I_{n_z\times n_z}\right)\hat{D}_L^{\gamma^*}, I_{n_y\times n_y}\right) P \\ &\operatorname{diag}\left(\left(\hat{D}_R^{\gamma^*}\right)^{-1}\operatorname{diag}\left(0I_{1\times1}, I_{n_p\times n_p}, \frac{1}{\sqrt{\gamma}} I_{n_w\times n_w}\right), I_{n_u\times n_u}\right)\end{aligned} \tag{54}$$

$$\begin{aligned}\hat{P}_N^{(k)} = \operatorname{diag}&\left(\operatorname{diag}\left(I_{1\times1}, I_{n_q\times n_q}, 0I_{n_z\times n_z}\right)\hat{D}_L^{N,k}, I_{n_y\times n_y}\right) P_N^{(k)} \\ &\operatorname{diag}\left(\left(\hat{D}_R^{N,k}\right)^{-1}\operatorname{diag}\left(I_{1\times1}, I_{n_p\times n_p}, 0I_{n_w\times n_w}\right), I_{n_u\times n_u}\right)\end{aligned} \tag{55}$$

  Output: Dynamic scaling transfer functions $\hat{D}^\bullet$ and scaled plants $\hat{P}_\gamma$, $\hat{P}_N^{(k)}$;
end

mance can be obtained by using formal robust synthesis methods such as μ-synthesis [46]. Besides, the low-order analytical model matching approach from Section 4 will no longer lead to satisfactory designs in the presence of high-order dynamics.[6] Design parameter optimization can resolve this [19].

In this section, the robust synthesis algorithm used to optimize the control designs from the previous section is discussed. This is followed by a brief introduction to the framework of Integral Quadratic Constraints (IQCs), which is used to extend the scope of robustness and performance analysis to the context of Linear Time-Varying (LTV) parametric uncertainties.

5.1. Synthesis algorithm

The multi-objective synthesis algorithm summarized in Algorithm 1 is used in this work. It relies on H_∞ formulations of the design requirements and boils down to an extended form of the DK-iteration approach used in μ-synthesis. The multi-model, multi-objective synthesis machinery offered by MATLAB® `systune` [47,10,48] forms the central element of the optimization routine. The combination of DK-iteration and parametric uncertainty sampling bears commonality with hybrid relaxation methods proposed in other studies [72,73]. Algorithm 1 makes the multi-disk synthesis functionality [74] from `systune` compatible with explicit incorporation of dynamic uncertainty in the design problem. As a result, robust disk stability margins such as those presented in [9] can be incorporated. Moreover, the multi-disk approach enables a distinction between nominal and robust design goals, as discussed in Section 3.2.

Due to its non-convex nature, there are no global optimality guarantees on the synthesis outcome. Therefore, the reliability of the result must be addressed by performing successive runs. Each run is initialized by a perturbed version of the design parameter returned by the last run, which gives an indication of sensitivity to initial conditions. These perturbations are performed randomly over a range up to 100%. This is accepted design practice [8].

5.2. Integral quadratic constraints

The framework of Integral Quadratic Constraints (IQCs) is a powerful instrument to perform formal robustness assessment of dynamic systems in the context of mixed uncertainty [75,76]. The framework enables relatively straightforward incorporation of time-varying uncertainties and nonlinearities. In this work, robustness against dynamic LTI, parametric LTI, and arbitrarily fast parametric LTV uncertainties is analyzed using appropriate multiplier descriptions as presented in [76]. The induced $\mathcal{L}_2$ gain serves as the performance metric. The IQClab[7] toolbox (3.00) [77] is used in combination with[8] YALMIP/MOSEK® (9.3.20) [78,79] to perform IQC-based worst-case performance assessment in MATLAB®.

6. Results

Robust synthesis is performed for all control law architectures from Section 4 and the operating conditions shown in Table 3. The benchmark PI controller is included as well. In this section, the synthesis results are evaluated. Moreover, the outcomes are used to reflect back on the equivalent regulation guidelines from Section 2.

6.1. Comparison of synthesis outcomes

The synthesis outcomes are evaluated in several ways. The relevant stability and performance properties achieved for the cruise condition are presented in Figs. 12-15. Numerical overviews of the corresponding synthesis data are provided in Tables 7-9. These list the worst-case margins with respect to the disk (Nichols) exclusion region from Section 3.2.3, the worst-case model-following performance compared to the desired level, and the corresponding design parameters. The values presented in these tables can be interpreted along the lines of standard well-posedness and boundedness arguments; that is, a criterion is robustly met if the associated worst-case gain does not exceed unity. Fig. 13 illustrates an example of what the LTI time domain stick step response envelope typically looks like, achieved by the PID control design in cruise. Fig. 14 shows how performance degrades in the presence of time-varying moment stability coefficients. These are modeled as:

$$M_\alpha(t) = M_\alpha\left(1 + w_{M_\alpha}\sin(t)\right), \quad M_q(t) = M_q\left(1 + w_{M_q}\sin(t + \tfrac{\pi}{2})\right) \tag{56}$$

[6] An extended pole placement strategy as presented in [5] could be exploited instead to resolve this issue.

[7] IQClab is made available by Novantec B.V. under a CC BY-ND 4.0 license; details on how to access the software can be found on https://www.iqclab.eu/.

[8] YALMIP is copyrighted material owned by Johan Löfberg and can be accessed via https://yalmip.github.io/. MOSEK® is a developed by MOSEK ApS; details on how to access the software can be found on https://www.mosek.com/.

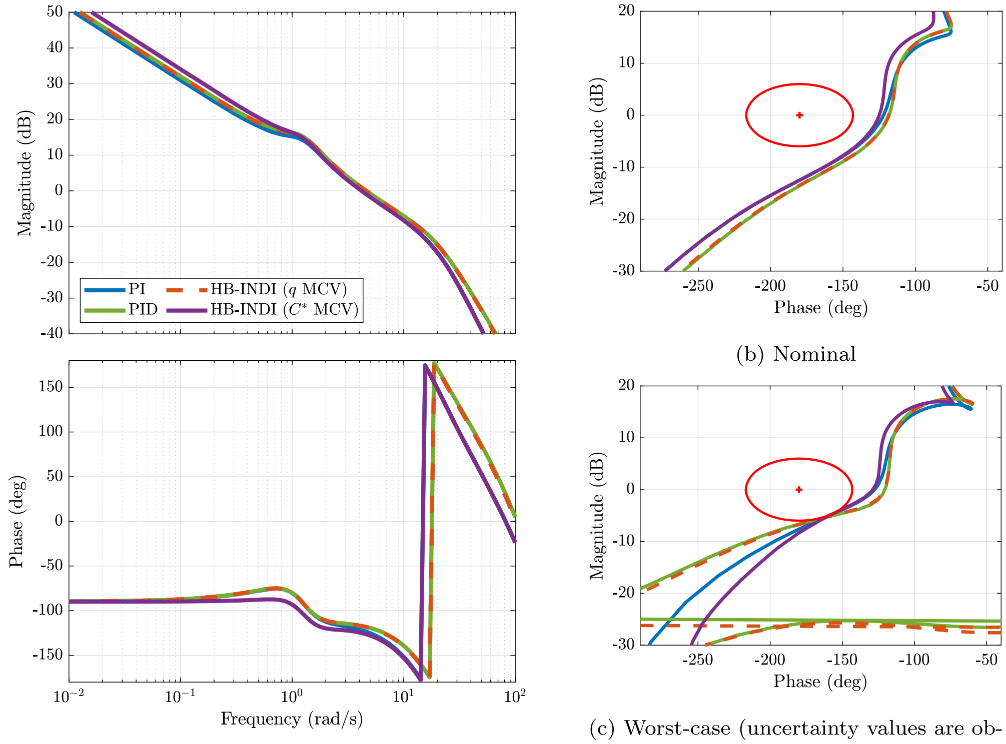

(a) Nominal

(b) Nominal

(c) Worst-case (uncertainty values are obtained using MATLAB® `wcgain`)

Fig. 12. Airframe input broken-loop frequency response (cruise).

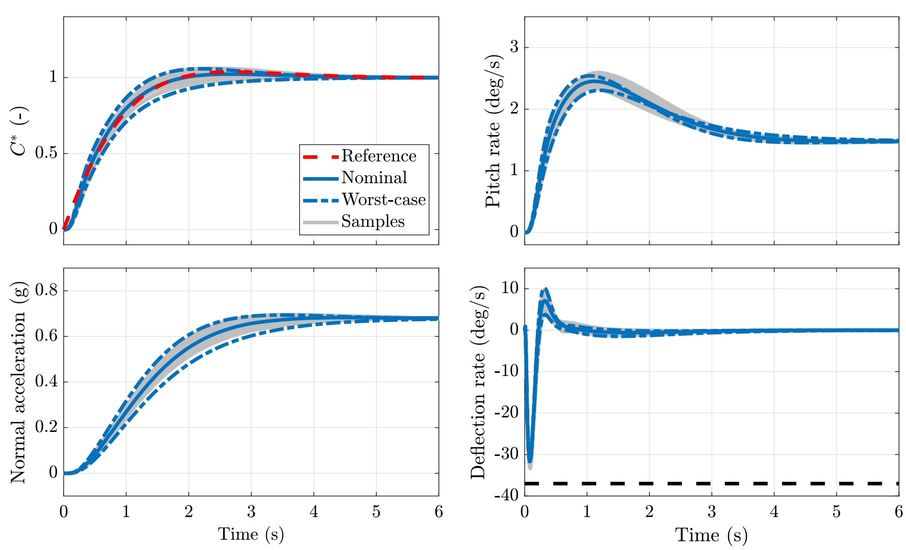

Fig. 13. Example of LTI response to step stick input (cruise; PID design). Monte Carlo samples are generated randomly within the set parametric uncertainty bounds; the upper and lower worst-case values are obtained using MATLAB® `wcgain`.

while $Z_\alpha(t) = Z_\alpha\left(1 + w_{Z_\alpha}\right)$ and $M_{\delta_e}(t) = M_{\delta_e}$. These variations do not reflect a realistic scenario *per se*. Rather, they must be considered as a single realization of the full LTV class; this provides further insight into relative LTV performance.

Altogether, the results show that all designs meet all hard design requirements and that they perform similarly in terms of the robust performance design objective. The PI architecture returns slightly lower robust performance levels compared to the other designs. The close connection between the PID and rate-inversion INDI control laws is apparent, as they result in identical response profiles at the selected flight conditions. The modular C^*-inversion design also results in similar robustness

Table 7
Worst-case disk margin H_∞-norms; the criterion is met for values up to and including 1.00 (returned by MATLAB® `wcgain`); see Fig. 4 for broken-loop locations.

	Cruise			Approach		
CLAW	Loc. A	Loc. B	Loc. C	Loc. A	Loc. B	Loc. C
PI	1.00	1.00	0.444	1.00	1.00	0.342
PID	0.993	0.994	0.442	1.00	1.00	0.342
INDI-q	0.993	0.993	0.442	1.00	1.00	0.342
INDI-C^*	1.00	1.00	0.473	1.00	1.00	0.360

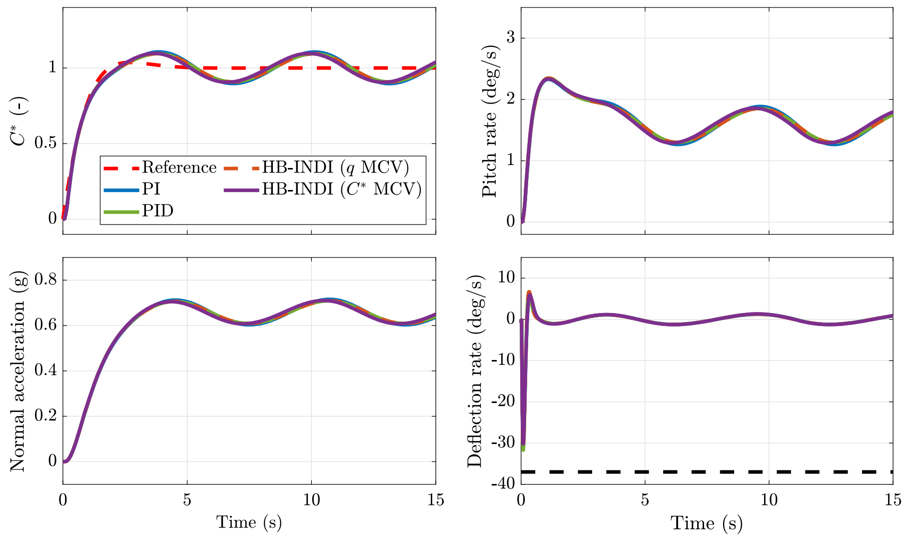

Fig. 14. Simulation of airframe response to step stick input (cruise) subject to LTV stability coefficient variations as per Equation (56).

Table 8
Worst-case model-following (MF) $\mathcal{L}_2$-gains.

	Cruise			Approach		
CLAW	MF (hybrid)	MF (`IQClab`)		MF (hybrid)	MF (`IQClab`)	
	LTI	LTI	LTV	LTI	LTI	LTV
PI	0.881	0.898	0.934	1.066	1.066	1.069
PID	0.794	0.807	0.932	1.007	1.007	1.042
INDI-q	0.800	0.813	0.926	1.011	1.011	1.040
INDI-C^*	0.832	0.832	0.899	0.793	0.793	0.831

Table 9
Synthesized design parameters.

Phase	CLAW	Regulator				Derivative/Inversion		
		K_f	K_i	K_p	K_q	$K_{\dot{q}}$	K_c	τ | τ_c
Cruise	PI	3.0	11.4	3.6	93	-	-	-
	PID	3.3	12.9	4.4	100	3.5	-	100
	INDI-q	0.08	0.44	0.22	2.0	-	0.09	100
	INDI-C^*	1.5	2.4	2.5	-	-	0.59	2.0
Approach	PI	3.0	15.2	6.8	165	-	-	-
	PID	3.3	16.6	7.8	177	5.8	-	100
	INDI-q	0.05	0.25	0.18	2.5	-	0.09	100
	INDI-C^*	1.0	1.1	1.7	-	-	0.96	2.0

levels. In cruise, this control law shows a slight performance deterioration compared to the PID design; on the contrary, better performance is achieved in the approach condition. Similar trends are observed for the LTV performance bounds returned by IQC analysis. This is verified by the simulation results in Fig. 14.

Summarizing, these results show no substantial distinction between the control laws from the perspective of LTI/LTV robustness and performance. This illustrates the effectiveness of both gain-scheduled PID and hybrid INDI design methods. Next, it is of interest to further investigate what hybrid INDI inversion error compensation contributes in terms of robustness. This concerns the modular design variant in particular. The following section reflects on this.

6.2. *Reflection on equivalent regulation in modular hybrid INDI*

To further understand how robustness is achieved by the modular hybrid INDI design from Section 4.3, it is instructive to reflect back on the principle of equivalent regulation outlined in Section 2. The connection to classical loop shape considerations is of particular relevance here. Broken-loop shapes are important indicators of robustness.[9] This is reflected by Fig. 12, which shows largely consistent loop shapes independent of control architecture. It is of interest to investigate how the concept of inversion error compensation contributes to these loop shapes.

Fig. 16a shows how the equivalent formulation relates to the uncompensated modular INDI design in terms of broken-loop singular values. This shows the net effect of the inversion compensation loop at low and high frequencies. The loop shape achieved by the uncompensated design is complemented by inversion error compensation to meet the robustness objectives. Therefore, robustness is improved separately from the outer (virtual control) loop. The concept of equivalent virtual control as described by Equation (13) has a useful implication in this context. Fig. 16b shows that the equivalent virtual control law behaves much like a PI compensator. This implies that the inversion compensation loop can be designed according to basic robust virtual control guidelines as presented in e.g. [23,28]. In the context of the first-order compensation architecture selected here, this gives rise to the following set of basic design guidelines:

$$K_c = 1 - \frac{K_i}{K_i^d} \tag{57}$$

$$\tau_c = \frac{1}{K_c}\left(K_p^d - K_p\right) \tag{58}$$

The superscript d stands for *desired*, which is clarified shortly. These equations are the result of low-frequency ($\omega \to 0$) and high-frequency ($\omega \to \infty$) response matching. The P/I-gains that correspond to the approximation in Fig. 16b take values of $K_p^d = 3.7$ and $K_i^d = 1.6K_p^d$, respectively. Substituting these values together with the actual virtual control gains from Table 9 yields $K_c = 0.59$ and $\tau_f = 2.0$, which is precisely the synthesis result.

Consequently, one can design *desired* equivalent virtual control gains based on robustness and convert them to inversion error compensation parameters. This shows how the inversion compensation loop maps to equivalent virtual control for robustness, while the actual virtual control is configured for flying-quality considerations only. Naturally, the level of inversion compensation needed depends on the level of robustness achieved through the outer loop. For example, $K_c = 1$ in case an integrator is absent. The loop crossover frequency is then dictated by the

[9] Of course, they have fundamental limitations with respect to MIMO systems and uncertainty. However, satisfactory robustness properties must be reflected by individual loops.

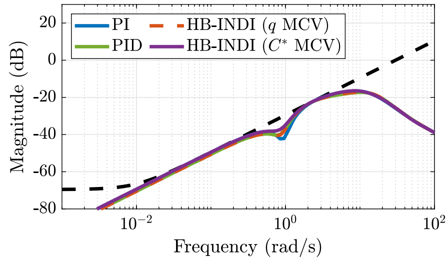

(a) Model-following error (nominal) compared to desired nominal performance (dashed)

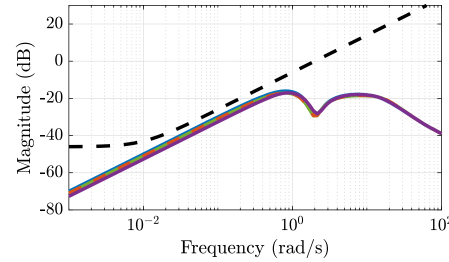

(b) Model-following error (worst-case) compared to desired robust performance (dashed)

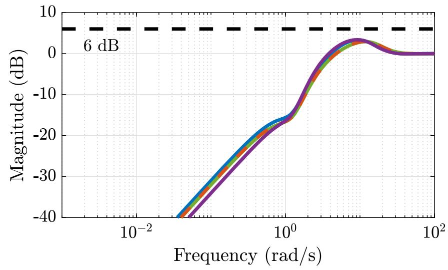

(c) Input sensitivity (nominal)

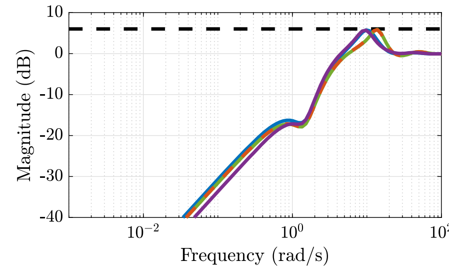

(d) Input sensitivity (worst-case)

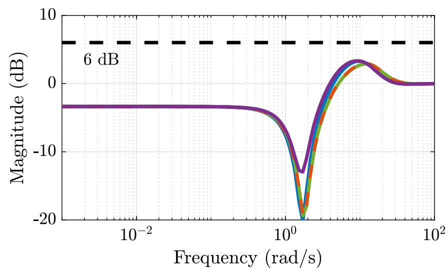

(e) Output sensitivity (q; nominal)

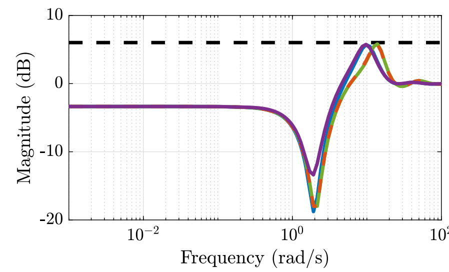

(f) Output sensitivity (q; worst-case)

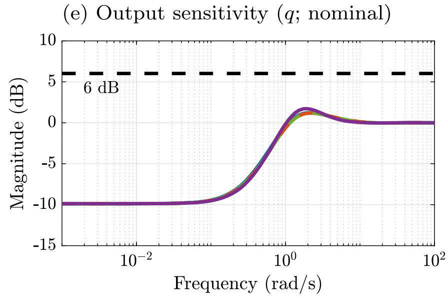

(g) Output sensitivity (n_z; nominal)

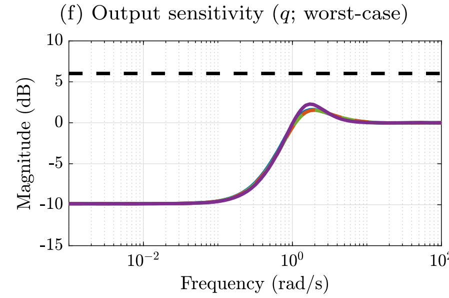

(h) Output sensitivity (n_z; worst-case)

Fig. 15. Robust performance frequency response diagrams (cruise); the worst-case values are obtained using MATLAB® `wcgain`.

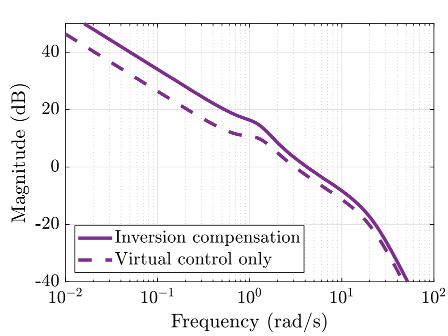

(a) Airframe input broken-loop

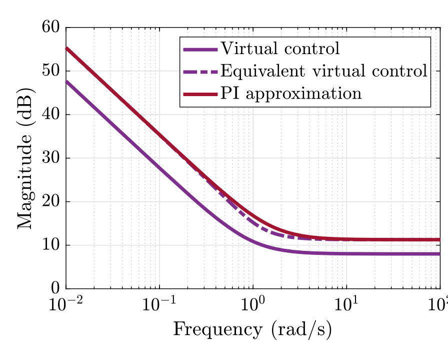

(b) Equivalent virtual control

Fig. 16. Effect of inversion error compensation in modular hybrid INDI design (C^* inversion).

compensation filter bandwidth. Moreover, if this bandwidth can be selected sufficiently large, one may choose to discard the on-board model (OBM) from the hybrid INDI control law altogether and implement a fully sensor-based design instead. These insights are useful to rapidly establish robust modular INDI designs; however, it is emphasized that a formal robust design framework is needed to optimize and guarantee robustness.

7. Conclusion

The objective of this study was to compare robust implicit model-following (IMF) flight control designs based on hybrid incremental nonlinear dynamic inversion (INDI) and gain-scheduled proportional-integral-derivative (PID) control. It has been shown that in the absence of high-order dynamics and uncertainty, there exists a direct equivalence between hybrid INDI design with rate inversion and gain-scheduled PID pole placement design in an LTI context. This close similarity is maintained in the presence of system perturbations after formal robust synthesis. In addition, it has been shown how the concept of hybrid INDI can be used to achieve modular IMF control designs in terms of flying qualities, robustness, and gain-scheduling. This gives rise to a nonlinear control law that has a transparent and transferable structure and achieves adequate robustness.

The insights from this work provide important answers to the question as to how hybrid INDI design and gain-scheduled PID control compare from a robust flight control design perspective. However, the synthesis framework was limited to an LTI context only. Considering the nonlinear nature of (I)NDI based control design, there is opportunity for improvement on this aspect. It is therefore suggested that Linear Parameter-Varying (LPV) synthesis methods are used in follow-up studies to further address this scenario.

Funding information

This research did not receive any specific grant from funding agencies in the public, commercial, or not-for-profit sectors.

CRediT authorship contribution statement

T.S.C. Pollack: Writing – original draft, Validation, Methodology, Investigation, Conceptualization. **S. Theodoulis:** Writing – review & editing. **E. van Kampen:** Writing – review & editing, Supervision, Funding acquisition.

Declaration of competing interest

The authors declare that they have no known competing financial interests or personal relationships that could have appeared to influence the work reported in this paper.

Data availability

Data will be made available on request.

Acknowledgements

The authors would like to thank dr. ir. J. Veenman from Novantec B.V. for providing access to the IQClab software suite; we also thank ir. M.H. Smaili for making the GARTEUR RECOVER Benchmark software package available.

References

[1] J.D. Blight, R.L. Dailey, D. Gangsaas, Practical control law design for aircraft using multivariable techniques, Int. J. Control 59 (1) (1994) 93–137, https://doi.org/10.1080/00207179408923071.
[2] M.B. Tischler, Advances in Aircraft Flight Control, Taylor & Francis, ISBN 978-0748404797, 1996.
[3] G.J. Balas, Flight control law design: an industry perspective, Eur. J. Control 9 (2) (2003) 207–226, https://doi.org/10.3166/ejc.9.207-226.
[4] S. Delannoy, S. Oudin, Longitudinal control law for modern long range civil aircrafts, in: Proceedings of the 2013 CEAS EuroGNC Conference, Delft, the Netherlands, 2013.
[5] S. Delannoy, Airbus generic control laws, in: Proceedings of the 2019 CEAS EuroGNC Conference, Milan, Italy, 2019, CEAS-GNC-2019-065.
[6] H.-D. Joos, A multiobjective optimisation-based software environment for control systems design, in: Proceedings of the IEEE International Symposium on Computer Aided Control System Design, Glasgow, UK, 2002, pp. 7–14.
[7] N. Moritz, R. Osterhuber, Three-Stage Gradient-Based Optimization Scheme in Design of Feedback Gains Within Eurofighter Primary Control Laws, AIAA Guidance, Navigation, and Control Conference and Exhibit, American Institute of Aeronautics and Astronautics, Keystone, CO, USA, 2006, AIAA 2006-6311.
[8] M.B. Tischler, T. Berger, C.M. Ivler, M.H. Mansur, K.K. Cheung, J.Y. Soong, Practical Methods for Aircraft and Rotorcraft Flight Control Design: an Optimization-Based Approach, American Institute of Aeronautics and Astronautics, ISBN 978-1624104435, 2017.
[9] D. Bates, I. Postlethwaite, Robust Multivariable Control of Aerospace Systems, DUP Science, ISBN 978-9040723179, 2002.
[10] P. Apkarian, P. Gahinet, C. Buhr, Multi-model, multi-objective tuning of fixed-structure controllers, in: 2014 European Control Conference (ECC), European Control Association, Strasbourg, France, 2014, pp. 856–861.
[11] A. Marcos, M. Sato, Flight Testing of an Structured H-Infinity Controller: An EU-Japan Collaborative Experience, 2017 IEEE Conference on Control Technology and Applications (CCTA), IEEE, Maui, HI, USA, 2017.
[12] W.J. Rugh, J.S. Shamma, Research on gain scheduling, Automatica 36 (10) (2000) 1401–1425, https://doi.org/10.1016/S0005-1098(00)00058-3.
[13] Anonymous, Flight Control Design - Best Practices, Tech. Rep. RTO-TR-029, NATO Research and Technology Organization (RTO), 2000.
[14] I. Kaminer, A. Pascoal, P. Khargonekar, E. Coleman, A velocity algorithm for the implementation of gain-scheduled controllers, Automatica 31 (8) (1995) 1185–1191, https://doi.org/10.1016/0005-1098(95)00026-S.
[15] R. Osterhuber, M. Hanel, R. Hammon, Realization of the Eurofighter 2000 Primary Lateral/Directional Flight Control Laws with Differential PI-Algorithm, AIAA Guidance, Navigation, and Control Conference and Exhibit, American Institute of Aeronautics and Astronautics, Providence, RI, USA, 2004, AIAA 2004-4751.
[16] H. Lhachemi, D. Saussié, G. Zhu, Handling hidden coupling terms in gain-scheduling control design: application to a pitch-axis missile autopilot, in: AIAA Guidance, Navigation, and Control Conference, American Institute of Aeronautics and Astronautics, San Diego, CA, USA, 2016, AIAA 2016-0365.
[17] G. Meyer, L.S. Cicolani, A formal structure for advanced automatic flight-control systems, Tech. Rep. NASA-TN-D-7940, National Aeronautics and Space Administration, Ames Research Center, Moffett Field, CA, USA, 1975.
[18] D. Enns, D. Bugajski, R. Hendrick, G. Stein, Dynamic inversion: an evolving methodology for flight control design, Int. J. Control 59 (1) (1994) 71–91, https://doi.org/10.1080/00207179408923070.
[19] G. Walker, D. Allen, X-35B STOVL flight control law design and flying qualities, in: 2002 Biennial International Powered Lift Conference and Exhibit, American Institute of Aeronautics and Astronautics, Williamsburg, VA, USA, 2002, AIAA 2002-6018.
[20] J.A. Franklin, Application of nonlinear inverse methods to the control of powered-lift aircraft over the low-speed flight envelope, Int. J. Control 59 (1) (1994) 321–335, https://doi.org/10.1080/00207179408923080.
[21] J. Bosworth, D. Enns, Nonlinear multivariable flight control, in: T. Samad, A. Annaswamy (Eds.), The Impact of Control Technology, 1st edition, IEEE Control Systems Society, 2011.
[22] C. Kim, C. Ji, G. Koh, N. Choi, Review on flight control law technologies of fighter jets for flying qualities, Int. J. Aeronaut. Space Sci. 24 (1) (2023) 209–236.
[23] Honeywell Technology Center, Lockheed Martin Skunk Works and Lockheed Martin Tactical Aircraft Systems, Application of multivariable control theory to aircraft control laws, final report: Multivariable control design guidelines, Tech. Rep., WL-TR-96-3099, 1996.
[24] H.-C. Oelker, R. Osterhuber, M. Hanel, Experiences with eurofighter handling qualities testing, in: AIAA Atmospheric Flight Mechanics Conference, American Institute of Aeronautics and Astronautics, Chicago, IL, USA, 2009, AIAA 2009-6321.
[25] J.J. Harris, J.R. Stanford, F-35 Flight Control Law Design, Development and Verification, in: 2018 Aviation Technology, Integration, and Operations Conference, American Institute of Aeronautics and Astronautics, Atlanta, GA, USA, 2018, AIAA-2018-3516.
[26] R. Hyde, G. Papageorgiou, Analysing the Stability of NDI-Based Flight Controllers with LPV Methods, AIAA Guidance, Navigation, and Control Conference and Exhibit, American Institute of Aeronautics and Astronautics, Montreal, Canada, 2001, AIAA 2001-4039.
[27] C. Papageorgiou, K. Glover, Robustness analysis of nonlinear flight controllers, J. Guid. Control Dyn. 28 (4) (2005) 639–648, https://doi.org/10.2514/1.9389.
[28] G. Papageorgiou, M. Polansky, Tuning a dynamic inversion pitch axis autopilot using McFarlane–Glover loop shaping, Optim. Control Appl. Methods 30 (3) (2009) 287–308, https://doi.org/10.1002/oca.864.

[29] R. Adams, S. Banda, Robust flight control design using dynamic inversion and structured singular value synthesis, IEEE Trans. Control Syst. Technol. 1 (2) (1993) 80–92, https://doi.org/10.1109/87.238401.
[30] J. Reiner, G.J. Balas, W.L. Garrard, Flight control design using robust dynamic inversion and time-scale separation, Automatica 32 (11) (1996) 1493–1504, https://doi.org/10.1016/S0005-1098(96)00101-X.
[31] S. Sieberling, Q.P. Chu, J.A. Mulder, Robust flight control using incremental nonlinear dynamic inversion and angular acceleration prediction, J. Guid. Control Dyn. 33 (6) (2010) 1732–1742, https://doi.org/10.2514/1.49978.
[32] C.-S. Kim, C.-H. Ji, G.-O. Koh, B.S. Kim, Stability margin and structural coupling analysis of a hybrid INDI control for the fighter aircraft, Int. J. Aeronaut. Space Sci. 22 (5) (2021) 1154–1169, https://doi.org/10.1007/s42405-021-00394-8.
[33] Y. Kumtepe, T. Pollack, E. van Kampen, Flight control law design using hybrid incremental nonlinear dynamic inversion, in: AIAA SciTech 2022 Forum, American Institute of Aeronautics and Astronautics, San Diego, CA, USA & Virtual, 2022, AIAA-2022-1597.
[34] T.J.J. Lombaerts, H.O. Huisman, Q.P. Chu, J.A. Mulder, D.A. Joosten, Nonlinear reconfiguring flight control based on online physical model identification, J. Guid. Control Dyn. 32 (3) (2009) 727–748, https://doi.org/10.2514/1.40788.
[35] C. Schumacher, Adaptive flight control using dynamic inversion and neural networks, in: Guidance, Navigation, and Control Conference and Exhibit, American Institute of Aeronautics and Astronautics, Portland, OR, USA, 1999, AIAA 1999-4086.
[36] C. Miller, Nonlinear dynamic inversion baseline control law: architecture and performance predictions, in: AIAA Guidance, Navigation, and Control Conference, American Institute of Aeronautics and Astronautics, Portland, OR, USA, 2011, AIAA 2011-6467.
[37] F. Grondman, G. Looye, R.O. Kuchar, Q.P. Chu, E. van Kampen, Design and flight testing of incremental nonlinear dynamic inversion-based control laws for a passenger aircraft, in: 2018 AIAA Guidance, Navigation, and Control Conference, American Institute of Aeronautics and Astronautics, Kissimmee, FL, USA, 2018, AIAA-2018-0385.
[38] F. Lavergne, Méthodologie de synthèse de lois de commandes non-linéaires robustes: Application au suivi de trajectoire des avions de transport, Theses, Université Paul Sabatier - Toulouse III, Oct. 2005, https://theses.hal.science/tel-00011557.
[39] F. Lavergne, F. Villaume, M. Jeanneau, S. Tarbouriech, G. Garcia, Nonlinear robust autoland, San Francisco, CA, USA, AIAA 2005-5848, https://doi.org/10.2514/6.2005-5848, 2005.
[40] E.J.J. Smeur, M. Bronz, G.C.H.E. de Croon, Incremental control and guidance of hybrid aircraft applied to a tailsitter unmanned air vehicle, J. Guid. Control Dyn. 43 (2) (2020) 274–287, https://doi.org/10.2514/1.G004520.
[41] A. Steinleitner, V. Frenzel, O. Pfeifle, J. Denzel, W. Fichter, Automatic take-off and landing of tailwheel aircraft with incremental nonlinear dynamic inversion, in: AIAA SciTech 2022 Forum, San Diego, CA, USA & Virtual, AIAA-2022-1228, 2022.
[42] T. Pollack, E. van Kampen, Robust stability and performance analysis of incremental dynamic-inversion-based flight control laws, J. Guid. Control Dyn. 46 (9) (2023) 1785–1798, https://doi.org/10.2514/1.G006576.
[43] E.J.J. Smeur, Q.P. Chu, G.C.H.E. de Croon, Adaptive incremental nonlinear dynamic inversion for attitude control of micro air vehicles, J. Guid. Control Dyn. 39 (3) (2016) 450–461, https://doi.org/10.2514/1.G001490.
[44] R. van 't Veld, E. van Kampen, Q.P. Chu, Stability and robustness analysis and improvements for incremental nonlinear dynamic inversion control, in: 2018 AIAA Guidance, Navigation, and Control Conference, American Institute of Aeronautics and Astronautics, Kissimmee, FL, USA, 2018, AIAA-2018-1127.
[45] R. Steffensen, A. Steinert, Z. Mbikayi, S. Raab, J. Angelov, F. Holzapfel, Filter and sensor delay synchronization in incremental flight control laws, Aerosp. Syst. 6 (2023) 285–304, https://doi.org/10.1007/s42401-022-00186-2.
[46] S. Skogestad, I. Postlethwaite, Multivariable Feedback Control: Analysis and Design, 2nd edition, John Wiley & Sons Ltd., ISBN 978-0470011683, 2005.
[47] P. Apkarian, D. Noll, Nonsmooth H_∞ synthesis, IEEE Trans. Autom. Control 51 (1) (2006) 71–86, https://doi.org/10.1109/TAC.2005.860290.
[48] P. Apkarian, M.N. Dao, D. Noll, Parametric robust structured control design, IEEE Trans. Autom. Control 60 (7) (2015) 1857–1869, https://doi.org/10.1109/TAC.2015.2396644.
[49] P. Apkarian, D. Noll, The H∞ control problem is solved, Aerospace Lab 13 (2017) 1–11, https://doi.org/10.12762/2017.AL13-01.
[50] H. Smaili, J. Breeman, T. Lombaerts, D. Joosten, A Simulation Benchmark for Integrated Fault Tolerant Flight Control Evaluation, AIAA Modeling and Simulation Technologies Conference and Exhibit, American Institute of Aeronautics and Astronautics, Keystone, CO, USA, 2006, AIAA 2006-6471.
[51] C. Edwards, T. Lombaerts, H. Smaili (Eds.), Fault Tolerant Flight Control: A Benchmark Challenge, Lecture Notes in Control and Information Sciences., Springer, Berlin, Heidelberg, ISBN 978-3642116896, 2010.
[52] C. van der Linden, DASMAT-Delft University Aircraft Simulation Model and Analysis Tool - A Matlab/Simulink Environment for Flight Dynamics and Control Analysis, Delft University Press, 1998.
[53] C.R. Hanke, The Simulation of a Large Jet Transport Aircraft. Volume 1: Mathematical Model, Tech. Rep. NASA-CR-1756, National Aeronautics and Space Administration, Ames Research Center, Moffett Field, CA, USA, 1971.
[54] C.R. Hanke, D.R. Nordwall, The simulation of a jumbo jet transport aircraft. Volume 2: Modeling data, Tech. Rep. NASA-CR-114494/D6-30643-VOL-2, National Aeronautics and Space Administration, Ames Research Center, Moffett Field, CA, USA, 1970.
[55] R. Brockhaus, Flugregelung, 2nd edition, Springer, Berlin, ISBN 978-3540418900, 2001.
[56] R.M. Hueschen, Development of the Transport Class Model (TCM) aircraft simulation from a sub-scale Generic Transport Model (GTM) simulation, Tech. Rep. NASA/TM–2011-217169, National Aeronautics and Space Administration, Langley Research Center, Hampton, Virginia, 2011.
[57] B. Stevens, F. Lewis, E. Johnson, Aircraft Control and Simulation: Dynamics, Controls Design, and Autonomous Systems, Wiley, 2015.
[58] E. Muir, The HIRM design challenge problem description, in: J.-F. Magni, S. Bennani, J. Terlouw (Eds.), Robust Flight Control: A Design Challenge, Springer, Berlin Heidelberg, Berlin, Heidelberg, 1997, pp. 419–443.
[59] G. Tauke, K. Bordignon, Structural coupling challenges for the X-35B, in: 2002 Biennial International Powered Lift Conference and Exhibit, Williamsburg, VA, USA, 2002, AIAA-2002-6004.
[60] Anonymous, Flying Qualities of Piloted Aircraft, U.S. Department of Defense, 1997, MIL-HDBK-1797A.
[61] D.G. Mitchell, R.H. Hoh, B.L. Aponso, D.H. Klyde, Proposed Incorporation of Mission-Oriented Flying Qualities into MIL-STD-1797A, Tech. Rep. WL-TR-94-3162, Wright Laboratory, Wright-Patterson AFB, OH, USA, 1994.
[62] C. Favre, Fly-by-wire for commercial aircraft: the airbus experience, Int. J. Control 59 (1) (1994) 139–157, https://doi.org/10.1080/00207179408923072.
[63] J. Hodgkinson, Aircraft Handling Qualities, Blackwell Science, Oxford, U.K., ISBN 978-0632038169, 1999.
[64] A. Zislin, E. Laurie, K. Wilkinson, R. Goldstein, X-29 aeroservoelastic analysis and ground test validation procedures, in: Aircraft Design Systems and Operations Meeting, American Institute of Aeronautics and Astronautics, Colorado Springs, CO, USA, 1985, AIAA 1985-3091.
[65] J. Harris, G. Black, F-22 control law development and flying qualities, in: 21st Atmospheric Flight Mechanics Conference, American Institute of Aeronautics and Astronautics, San Diego, CA, USA, 1996, AIAA 1996-3379.
[66] R. Steffensen, A. Steinert, F. Holzapfel, Incremental control as an enhanced and robust implementation of gain scheduled controllers avoiding hidden coupling terms, Aerosp. Sci. Technol. 141 (2023) 108500, https://doi.org/10.1016/j.ast.2023.108500.
[67] H. Khalil, Nonlinear Systems, 3rd edition, Prentice Hall, ISBN 978-0130673893, 2002.
[68] G. Looye, H.-D. Joos, Design of robust dynamic inversion control laws using multi-objective optimization, in: AIAA Guidance, Navigation, and Control Conference and Exhibit, American Institute of Aeronautics and Astronautics, Montreal, Canada, 2001, AIAA 2001-4285.
[69] P. Gahinet, P. Apkarian, Automated tuning of gain-scheduled control systems, in: 52nd IEEE Conference on Decision and Control, IEEE, Firenze, Italy, 2013, pp. 2740–2745.
[70] Anonymous, Control System Toolbox™ Reference, The MathWorks, Inc., 2024.
[71] G. Balas, R. Chiang, A. Packard, M. Safonov, Robust Control Toolbox™ User's Guide, The MathWorks, Inc., 2021.
[72] R.S. da Silva de Aguiar, P. Apkarian, D. Noll, Structured robust control against mixed uncertainty, IEEE Trans. Control Syst. Technol. 26 (5) (2018) 1771–1781, https://doi.org/10.1109/TCST.2017.2723864.
[73] B. Patartics, G. Lipták, T. Luspay, P. Seiler, B. Takarics, B. Vanek, Application of structured robust synthesis for flexible aircraft flutter suppression, IEEE Trans. Control Syst. Technol. 30 (1) (2022) 311–325, https://doi.org/10.1109/TCST.2021.3066096.
[74] P. Apkarian, D. Noll, Nonsmooth optimization for multidisk H_∞ synthesis, Eur. J. Control 12 (3) (2006) 229–244, https://doi.org/10.3166/ejc.12.229-244.
[75] A. Megretski, A. Rantzer, System analysis via integral quadratic constraints, IEEE Trans. Autom. Control 42 (6) (1997) 819–830, https://doi.org/10.1109/9.587335.
[76] J. Veenman, C.W. Scherer, H. Köroğlu, Robust stability and performance analysis based on integral quadratic constraints, Eur. J. Control 31 (2016) 1–32, https://doi.org/10.1016/j.ejcon.2016.04.004.
[77] J. Veenman, C.W. Scherer, C. Ardura, S. Bennani, V. Preda, B. Girouart, IQClab: a new IQC based toolbox for robustness analysis and control design, in: 4th IFAC Workshop on Linear Parameter Varying Systems LPVS 2021, IFAC-PapersOnLine 54 (8) (2021) 69–74, https://doi.org/10.1016/j.ifacol.2021.08.583.
[78] J. Lofberg, YALMIP: a toolbox for modeling and optimization in MATLAB, in: 2004 IEEE International Conference on Robotics and Automation, IEEE, Taipei, Taiwan, 2004, pp. 284–289.
[79] Mosek ApS., MOSEK Optimization Toolbox for MATLAB 9.3.20, Available online https://docs.mosek.com/9.3/toolbox/index.html, 2023.